

LA-UR-19-25117

Approved for public release; distribution is unlimited.

Title: Internship Report: Numerical modelling of impact seismic signals on regolith

Author(s): Froment, Marouchka

Intended for: Report

Issued: 2020-01-15 (rev.2)

Disclaimer:

Los Alamos National Laboratory, an affirmative action/equal opportunity employer, is operated by Triad National Security, LLC for the National Nuclear Security Administration of U.S. Department of Energy under contract 89233218CNA000001. By approving this article, the publisher recognizes that the U.S. Government retains nonexclusive, royalty-free license to publish or reproduce the published form of this contribution, or to allow others to do so, for U.S. Government purposes. Los Alamos National Laboratory requests that the publisher identify this article as work performed under the auspices of the U.S. Department of Energy. Los Alamos National Laboratory strongly supports academic freedom and a researcher's right to publish; as an institution, however, the Laboratory does not endorse the viewpoint of a publication or guarantee its technical correctness.

Internship Report: Numerical modelling of impact seismic signals on regolith

Marouchka Froment

Abstract

In November, 2018, the Insight mission deployed the first seismometer on the surface of Mars, which is returning seismic data since January 2019. Mars tectonic activity is expected to be low, making meteorite impacts an important source of seismic signal. It is thus necessary to develop models of the amplitude and frequency content of the seismic signal they generate. During this internship, the HOSS (Hybrid Optimization Software Suite) mechanical simulation software of the Los Alamos National Laboratory (LANL) was used to model the dynamics of hypervelocity impacts on a regolith layer. An original model for low density porous medium was developed on the basis of small-scale experiments targeting a pumice sand, conducted at the NASA Ames Vertical Gun Range (AVGR) facility. A parametric study was made to understand various features of the equation of state and strength equation of the target material. The transition between the elastic the plastic regime of the equation of state was shown to have a big influence on the amplitude and shape of an impact-induced shock wave. Taking a transition pressure of $P_{el} = 10^3$ Pa, an elastic bulk modulus of $K_{el} = 10$ MPa and a transition bulk modulus of $K_{trans} = 6$ MPa showed a good agreement of the velocity and acceleration signal between the numerical model and the experimental results. In future works, this model will be used to study impact seismic sources at larger scales and their analogy with recent marsquakes recorded by InSight's seismometer.

Keywords: Planetary Sciences, Shock Physics, Impacts, Seismology, Mars

Contents

1	Introduction	2
2	Setting up and validating a numerical model of the Martian regolith	5
2.1	Methodology, available tools and data	5
2.2	Tests on the EOS and H7H : presentation, results and analysis	13
2.3	Creation of the regolith model	20
2.4	Limitations of our study	22
3	Conclusion	27
4	Acknowledgments	27
A	Example of Shot #13 data	30

1 Introduction

Mars: a quiet planet ?

Mars is the fourth telluric planet of our solar system. It is half the size of Earth in radius and orbits at around 1.5 astronomic units from the sun. It is therefore a small, cold object with a faint atmosphere. However, these characteristics are also the reason why it is an important subject of study. Thanks to the planet's small mass and faint atmosphere, Mars' surface can be observed from orbit by optic instruments and is within reach of today's landers. Since the first soviet mission Mars 2 in 1971, it hosted 10 landers and rovers carrying out geologic experiments. Moreover, Mars is closer to the Earth in size and mass than the Moon and other reachable objects of the solar system. By studying the history of Mars and comparing it to Earth's, the scientific community gathers evidence to test modern scenarios of the formation and evolution of telluric planets in the solar system, and challenges hypotheses about their ability to host life.

Over the last century, many discoveries were made on Mars, and old popular beliefs on the existence of its flora and fauna were blown away. Today, Mars is considered to be free of any trace of biologic life. Mars' tectonic life is thought to be lower than Earth's and may even be gone for good [Zuber et al., 2000]. Its global magnetic fields is also weak (< 0.5 nT) and dominated by crustal sources [Connerney et al., 2001]. Consequently, little is known on its interior structure and evolution. Mars' surface, however, shows a high number of old and more recent meteorites impacts. This impacting activity can even be monitored through analysis of the satellite Mars Reconnaissance Orbiter (MRO) image bank [Daubar et al., 2014]. Measuring Mars' tectonic and meteoritic activity, and using it to study the interior structure of the planet, is now one of the science objectives of the InSight (Interior Exploration using Seismic Investigations, Geodesy and Heat Transport) lander.

The InSight mission

The Insight mission landed on Mars on November 26, 2018. It is equipped with a short period and a very broadband seismometer, SEIS (Seismic Experiment for Interior Structure) [Lognonné et al., 2019], developped at the Centre National d'Études Spatiales (CNES) and Institut de Physique du Globe de Paris (IPGP). SEIS was placed on the surface of the planet in December 2018 and has been, since then, "listening" on the Martian soil as a part of its 2-year mission.

Over the first three months of its operation, SEIS recorded four likely "marsquakes" (NASA Press Release - 19-032). With a single seismic station and little knowledge of the internal structure of the planet, it is difficult to assess with precision the exact origin of a signal. The later could be coming from small faults or old geologic formation in the lander's close environment, or from contraction caused by the planet's cooling. It could also be produced by volcanic activity, by a landslide, and last by meteoritic activity. All of these hypotheses have to be investigated with precision while scientists are waiting for more events to conduct statistic studies. This work is focusing on the impact origin.

The impact cratering physics: an active area of research

In this framework, it is important to have a full understanding of the physics behind the seismic excitation of impacts. An interesting aspect of impacts is that their location can be established with satellite image of orbiters such as MRO. Satellite image will also provide information on the size of the crater, that would be an important constraint to the impact physics. However, the dynamic process of generating seismic waves from meteorite impacts is still unknown in large

part. Available data is limited to laboratory experiments on Earth and to information collected on terrestrial impacts (occurring in Earth atmospheric condition) and lunar impacts recorded by the Apollo mission (occurring without atmosphere).

Five seismometers were placed on the surface of the Moon in the late 60's to early 70's, during the Appolo 11, 12, 14, 15 and 16 missions. They recorded man-made impacts like of the Lunar Module (LEM) and determined a relationship between signal amplitude and impact distance. These relationships may be applied to Martian events, for instance events of Sols 105 and 133 (see figure 1). However, no existing theory can predict the spectrum and cutoff frequency of these events' signal. Appolo data cannot constrain the source, whose information is lost during propagation. This knowledge of the source is of critical importance to be able to discriminate between impact events and other possible origins of signals detected by SEIS.

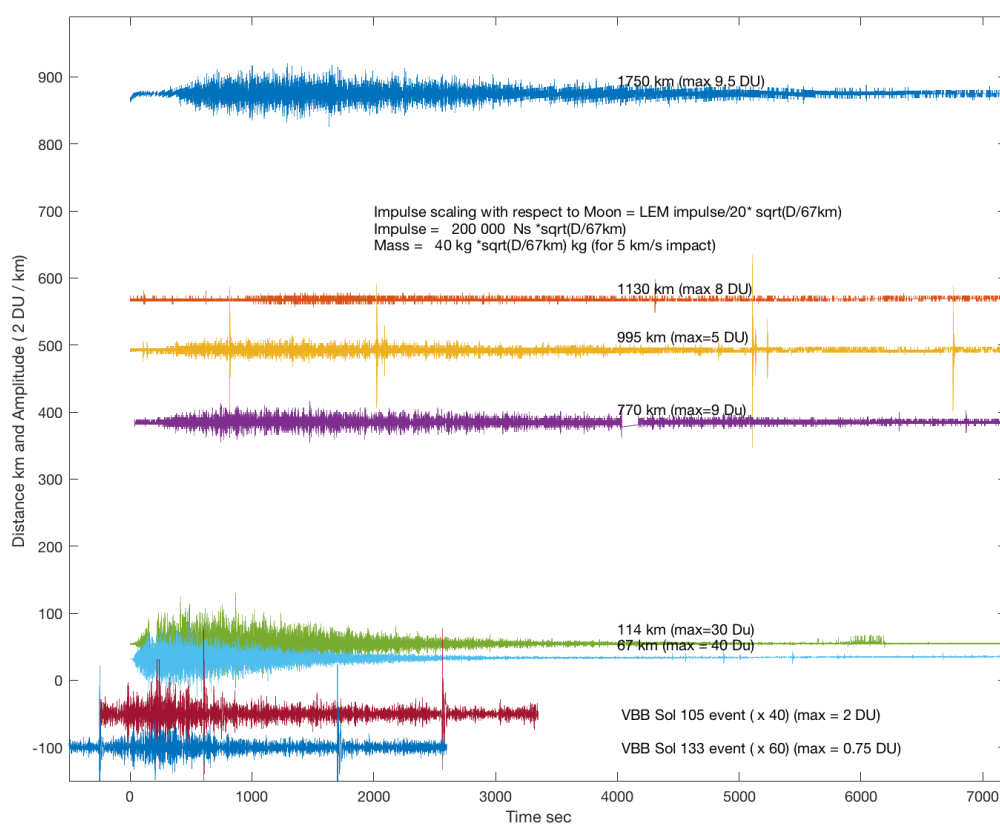


Figure 1 – Signals of the LEM impacts recorded by Appolo seismometers compared to *Sol 133* and *Sol 105* Martian signals. Respective amplitude are converted to Appolo's Digital Units (DU) and used to determine the possible distances of events 133 and 105. Pers. comm. of P. Lognonné.

During an impact event, several high-energy phase transitions, deformation and failure phenomena take place. The dynamics of these phenomena is hard to model or even to reproduce in laboratory experiments. Observation of terrestrial crater geology has shown that a significant amount of melting and vaporizing may take place in the very first seconds of an impact shock [Melosh, 1989]. The kinetic energy of the bolide hitting the ground then transfers into a shock wave, which will induce a non-linear plastic response of the medium it propagates in. The dissipation of this shock wave through viscous damping phenomena, and geometric spreading

will finally allow the shock wave to reach a linear-elastic state and propagate as a seismic wave. The exact amount of energy that is transferred from the bolide to this seismic wave is not well constrained. The *seismic efficiency*, described as the ration of seismic energy over the initial kinetic energy of an impact, varies from 10^{-6} to 10^{-2} [Güldemeister and Wünnemann, 2017]. The wave's amplitude, shape and frequency components will highly depend on the bolide and the ground mechanical and thermodynamical properties.

Therefore, a better understanding of the dynamics of impacts in materials with different geological properties is the key to better assess their associated seismic source.

Aim of the work

Most of the shallow surface of the Moon and Mars around the InSight lander is known to be covered with regolith, an unconsolidated mix of sand and small fractured rocks covering a wide range of grain sizes. Due to its grainy structure, sand undergoes a very different evolution than bedrocks under strong load. Contrary to rocks, which will dissipate the loaded energy mainly through elastic deformation and fracture, sand will dissipate a significant amount of energy through the process of pore-crushing, compaction, friction and grain displacement. This dissipative property explains why sandy materials are often used as protections against shocks. Also for this reason, sands and unconsolidated materials are thought to show a very different response under hypervelocity impacts. In the context of planetary exploration and the InSight mission, it has become necessary to understand what kind of signal, amplitudes and frequencies an impact in regolith could produce.

Moreover, a planetary surface cannot be described by a single layer of regolith. Close to the InSight lander, this layer is thought to vary between 2 and 12 meters depth [Warner et al., 2017]. In addition to the previous question, an exhaustive study of impact seismic source should thus also take into account a layer of basaltic bedrock lying below the unconsolidated material. This second layer might undergo fracturing and plasticity above a range of impactor sizes, speeds and regolith depth. The effect of these plastic response to the impact shock have never been investigated.

To answer this question, small-scale laboratory experiments are not sufficient. On the other hand, the theory of impact physics is limited, given the extremely non-linear phenomenon at play during the shock. However, both these areas of impact physics may help build an accurate numerical model, able to describe shock waves both at small and large scales. Many of such codes, called hydrocodes or shock codes, have been developed over the years, and they have recently shown a good consistency with some laboratory experiments and between them in benchmarking exercises [Pierazzo et al., 2008]. Still, a lot of them remain limited to the description of continuous materials similar to fluids, and struggle to handle fracturing and grain-like behaviours of geomaterials [Güldemeister and Wünnemann, 2017].

This Master internship aims at using a novel numerical modelling software, HOSS (Hybrid Optimization Software Suite), developed at the Earth and Environmental Sciences division of the Los Alamos National Laboratory [Munjiza et al., 2014], to create a model of impacts on regolith. This software is able to simulate high strain and high stress situations using first principle physics. It is also able to handle fractures and discontinuities in a unique way, which makes it fit for an accurate description of geomaterials. By designing a representative model of the Martian subsurface, it will allow for the determination of the medium's influence on the seismic signal produced by impacts, and thus to verify the estimates of Daubar et al. [2018] and Teanby [2015].

To accurately calibrate the model of regolith, a set of reduced-size experiments of supersonic impacts conducted in 2012 at the NASA-AVGR (Ames Vertical Gun Range) facility [Richardson

and Kedar, 2013] was first used. Several parametric studies were conducted in order to understand the role of each part of the model. Then, the results of these studies were applied to the determination of an accurate model of regolith for the experiments. This model will allow for the simulation of impacts at bigger scales, for future comparison and analysis of data recorded by SEIS.

2 Setting up and validating a numerical model of the Martian regolith

2.1 Methodology, available tools and data

To create a trustworthy numerical model of a physical phenomenon, two steps have to be followed. In a first step, the numerical tool itself has to go through the process of *Verification*, which is making sure that it yields physical results and solves a set of conservation equations correctly. Once confidence in the numerical solver is gained, the second process is the *Validation* of the model. It consists in testing the chosen model against real-world solutions, in a certain regime. To do this, several simulations should be set up to reproduce laboratory experiments, and their results should be compared to the field data. In an ideal case, several codes should be benchmarked, which makes it possible to compare their results, confront and extend theory in regimes where validation is not possible because experimental data is lacking.

Most of the existing numerical tools have already been carefully verified. This is also the case for HOSS. However, models of a variety of geomaterials still need to be built and validated. The Earth and Environmental Science Division of LANL was designing a model of sand before the beginning of this project, but its validation process was not finished. The first part of this internship thus consisted in the validation of a sand model for regolith. During a two and a half months visit to LANL, I learnt how to handle HOSS and designed the appropriate setups for this work. The validation process used the yet unpublished data from hypervelocity impacts experiments, conducted at AVGR in 2012. The following sections are a descriptions of the numerical tool, the experimental data and literature that were used to build this model.

2.1.1 The principle of a FDEM simulation

Historically, numerical codes designed to investigate shock physics used to study the hydrodynamic behavior of materials, and most of nowadays "shock physics" solver are therefore still called *hydrocodes*. The original hydrocodes solved the equations of conservation of mass, momentum and energy, but today's shock codes are also able to handle the constitutive equations of materials. These constitutive equations are generally separated into the *volumetric* (equation of state, further referred as EOS) and the *deviatoric* (strength model) response of a media (e.g Pierazzo et al. [2008]).

Whereas the conservation equations remain the same for all hydrocodes, the constitutive equations and the way the conservation equations are formulated differ from one code to another. As reported in Pierazzo et al. [2008], the two main formulations are the *Eulerian* formulation and the *Lagrangian* formulation, along with some hybrid solutions. In the Eulerian formulation, the simulation mesh is fixed and the materials flows through it. This means that interfaces and discontinuities will be smoothed and limited by the element size. Tracking these discontinuities may become a problem. The Lagrangian formulation fixes the grid on the material elements. The mesh is carried along with it, which makes interface tracking very easy. However, elements might deform too much in high-strain region and cause inaccuracy in the integration of conservation equations.

HOSS was developed at LANL to provide an innovative solution for simulating discontinuities.

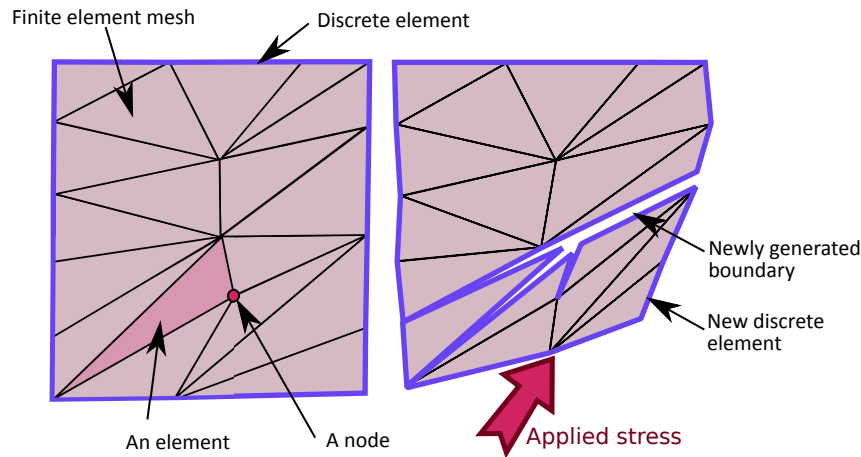


Figure 2 – Graphic of a block of elements before and after a fracture, showing its finite and discrete element mesh

The Finite-Element method is used in the resolution of continuous deformation inside of a group of elements. But interfaces and frontiers between elements are described by the Discrete-Element Method, as shown in figure 2 [Munjiza et al., 2014]. This allows the software to simulate bounding forces between elements, damage, and fracture. The Discrete-Element mesh also handles contact detection between several elements.

2.1.2 HOSS input models and controllable parameters

As LANL is a United States Department of Energy National Laboratory, HOSS source code is limited to the development team. For this reason, it is not available to users outside of the development team. However, HOSS' inputs and several parameters can be modified by regular users. They are several added *.input* files, which contain the model to be used. Here is their description:

mesh.input The geometry of the simulation is generated using the software *Cubit*, designed at Sandia National Laboratory. This software enables to create any type of 3D or 2D geometry and mesh it with relatively versatile element sizes. It then generate an *abaqus* file, that can be translated to HOSS' language. The *mesh.input* file contains the coordinates of all elements and element nodes, classified into several respectively *blocks* and *nodesets*. A block gathers all elements that are part of the same material. A nodeset gathers all nodes that will be subjected to particular boundary or initial conditions.

MPIDomains.input Once the geometry has been generated, it is sliced into several MPI domains for parallelisation. The user defines the extent of the total domain, and the mean number of element per MPI domain. For HOSS simulations, MPI domains should contain between 1000 and 3000 elements, which results in a few hundreds of MPIDomains.

xxx.input The *xxx.input* file contains all the simulation informations that will be needed by HOSS and are controllable by the user. The simulation duration, timestep and output samplings are defined in this file. It also attributes a particular solver to each block, depending whether the simulation is 3D or 2D, whether the material contains cohesive properties or is simply continuous. The *xxx.input* file also allows to define the position of the *sensors* the user wants to get as outputs. Sensors are lumped into an element, at the initial time. Each sensor will be saved as a text file displaying coordinates, velocity and stress tensor elements at each time at the sensor position. Finally, the *xxx.input* file gathers some inputs files *bc.input*, *EOS.input* and *H7H.input* containing boundary conditions, initial conditions and constitutive equations of each block and nodeset.

bc.input The *bc.input* file includes the boundaries and initial conditions attributed to each nodeset. It will also fix the cohesive properties of each block of elements. These cohesive properties include the friction coefficient between two elements, and a damage law if they are linked together by a breakable bound.

EOS.input, H7H.input These two inputs are specific to this particular project. The *EOS.input* is a file containing the curve of the volumetric response of a particular material. *H7H.input* contains the strength/mean-stress curves describing the deviatoric response of a particular material. In a regular project with purely elastic material, these constitutive equation can simply be defined in the *xxx.input*. Here, an EOS and strength equation can be designed separately for greater flexibility. The curves of the deviatoric and volumetric response are determined by a number of physical parameters (bulk modulus K_{el} , shear modulus G , transition pressure P_{el} from an elastic to a plastic behaviour...). This modelling work implied mostly finding a set of these parameters, which will be described more precisely in section 2.1.4.

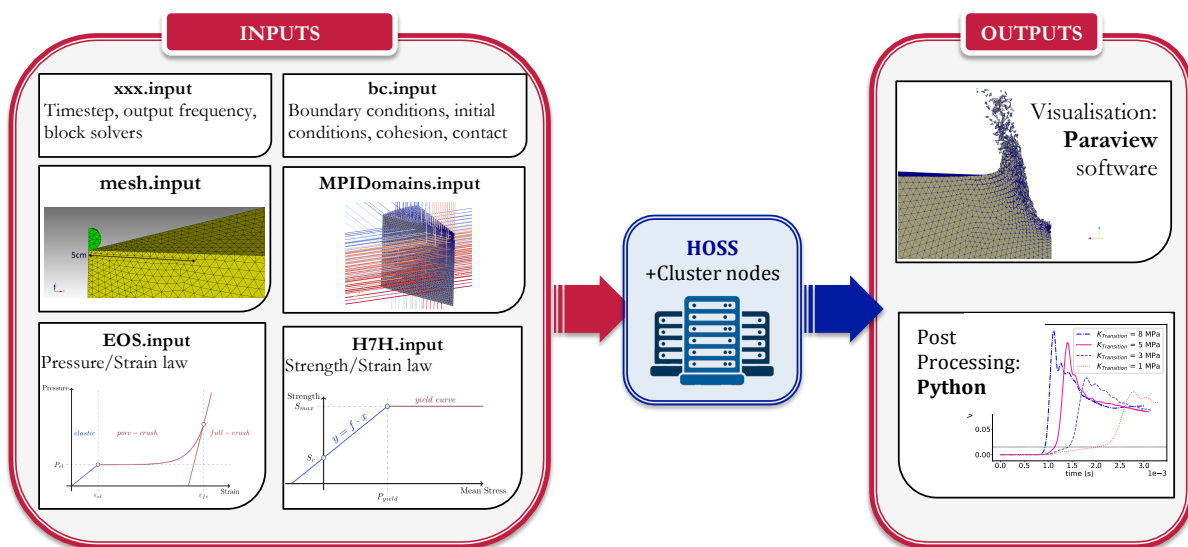


Figure 3 – Diagramm of all HOSS inputs and outputs.

This set of modifiable parameters are schematized on figure 3. The simulation outputs sensor files and *.vtu*, *.pvtu* files that can be visualised with the software *Paraview*, from the Sandia National Laboratory. During this internship, the sensor data were post-processed using *Python*. *Paraview* helped viewing the velocity and stress field, crater and ejecta shape, as well as determining the cause of some crashes and problems.

2.1.3 Experimental data

In June 2012, Dr. J. E. Richardson and S. Kedar conducted a set of 22 laboratory hypervelocity impacts experiments. [Richardson and Kedar, 2013]. These experiments used the NASA Ames Vertical Gun Range (AVGR), a facility capable of shooting small bolides over a wide range of velocities and angles, in a highly controlled environment. The last of such experiments had occurred around 50 years ago and did not provide the high precision and sampling rates of today's sensors [McGarr et al., 1969].

The experimental setup is a closed tank, 2 meters in diameter and in height, filled with a controlled atmosphere and target bed. In this set of experiments, Drs. Richardson and Kedar were interested in the impact induced seismic signals generated on the shallow surface of low-atmosphere planets by small bolides. They thus conducted 11 experiments in a near

Shot #	Impact angle from horizon (°)	Impact velocity (km/s)	Impactor type	Impactor mass (g)	Pressure, Pa (% of Mars atmosphere)
13	90	0,98	pyrex	0,2965	584,0 (97%)
22	90	5,82	aluminum	0,3765	653,4 (109%)

Table 1 – Characteristics of the two shots available for this study.

vacuum (Pressure lower than 1.0torr (130 Pa)), similar to the Moon atmosphere; and 11 other experiments in a Martian atmosphere of ~5-10 torr (660. - 1300 Pa). The Moon-like experiments used a 0.1 – 0.2mm sand grains target bed, whereas the Mars experiments used a pumice sand target bed of similar grain size.

Tests were monitored by 15 accelerometers buried into the sand, with a sampling rate of 10^{-5} s. Three stations buried vertically from the impact points recorded the vertical acceleration. The remaining station were buried in varied positions radially from the impact points and recorded both the vertical and radial acceleration. The AVGR was also equipped with 4 cameras with similar sampling rates, which were triggered a few milliseconds before the impact time. These camera provided information on the crater ejecta angle and growth rate. By imaging the burst of plasma produced at the contact of the bolide with the test bed, they could also provide a precise measure of the time of impact. Finally, the crater sizes and profiles were also measured at the end of the tests.

This project being linked to Martian seismology, only the tests conducted in a pumice test-bed with a Mars-like atmosphere were used in this study. This pumice sand medium was chosen to be similar in composition, grain size, and density to the Johnson Space Center (JSC) Mars-1 Regolith Simulant [Allen et al., 1997]. Among the 11 tests made with this material, 6 were made with a vertical incidence of the bolide and impact velocities ranging from 0.98 to 5.2 km/s. The 5 other shots were conducted with a 3.0 km/s velocity and incidence angles ranging from 15 to 75 degrees. All shots used a 6.3 mm radius pyrex bead as impactor, except the highest velocity one which used an aluminium bead of the same radius. Their mass were respectively 0.29g and 0.37g. Pictures of the ejecta, crater and testbed of Shot #22 are shown on figure 5.

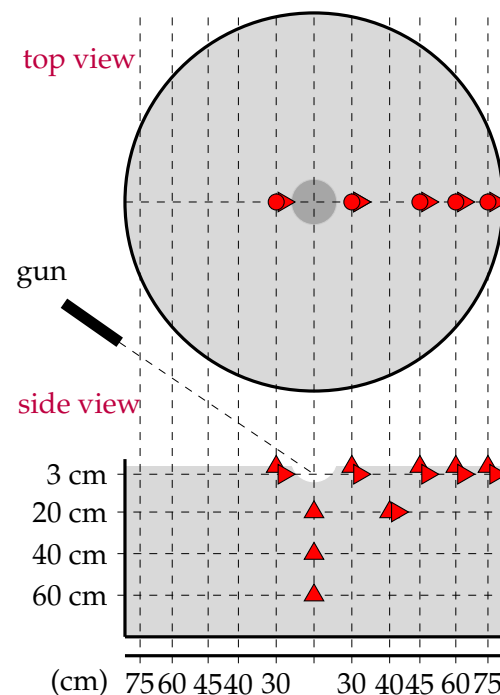


Figure 4 – Description of the experimental setup of the AVGR experiments

At the beginning of this project, only the data of shot #22, the highest velocity impact, were available to the team. We then received the data of Shot #13, the lowest velocity impact on pumice. We have conducted our study using only these two impacts, which cover the minimum and maximum simulated impact energies. However, Shot #13 low impact velocity made simulation more stable, and was more used than Shot #22 when numerous tests were needed. The precise characteristics of these two shots are summarized in table 1, and some of the data of Shot #13 are shown in appendix A.

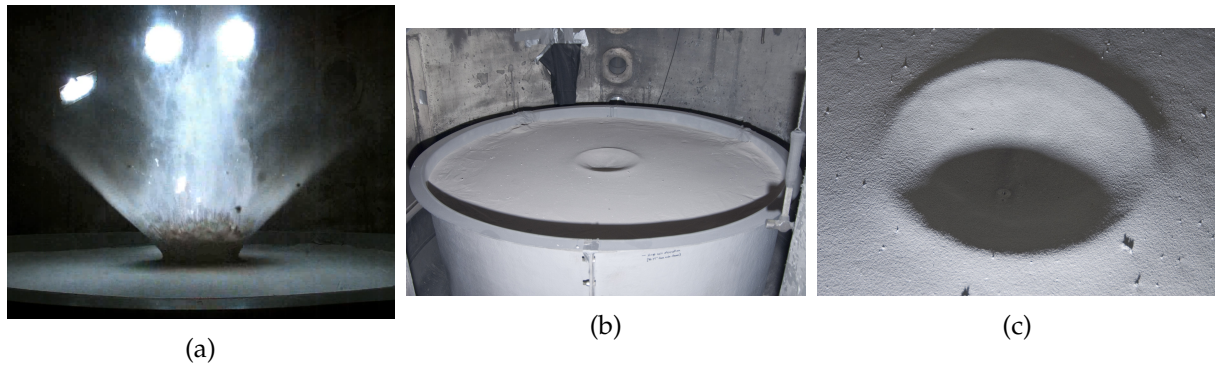


Figure 5 – (a) Screenshot of Shot #22 side-view movie, 26ms after the impact. (b and c) Illustration of the resulting 17.4cm radius crater.

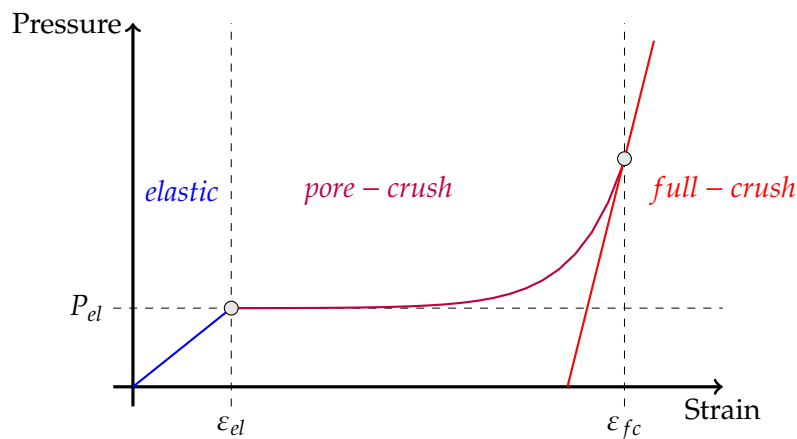


Figure 6 – Description of the typical Equation of State of a sand material

2.1.4 Litterature data and geomechanics

Before going any further, the mechanics of sands under shocks needs to be described. Sands are unconsolidated, grainy materials. Sand grains present a variety of shapes and sizes, which causes their piling and stacking to be imperfect and creates empty volumes filled with gas, called *pores*. When submitted to a weak loading, a sand material will respond elastically, as the supplied energy is not big enough to deform the pores or the grains permanently. Above a certain loading, part of the loading energy goes into rearranging the grains with respect to each other, and fills some of the pores : the material is no longer elastic. Under higher loading, sand grains will start to split into finer grains, filling the pores even more. This pore-crushing behaviour absorbs a large portion of the loading energy. Finally, at the end of this crushing process, all pores disappear, and sand grains are in complete contact with one another. At this pressure, sands behaves like a stone made of the same minerals.

This empirical description of sand may be formalised using the usual properties of continuum mechanics : strain and stress, applied to a mesoscopic material element containing several grains of sand. In the case of sand and many geomaterials, stress-strain relationships are divided in two : the *volumetric* and *deviatoric* behaviour.

The volumetric constitutive law, or Equation of State (EOS), describes how pressure P will be linked to the volumetric strain ε_v . We have :

$$P = f(\varepsilon_v) \quad \text{and} \quad \varepsilon_v = \frac{V_0 - V}{V_0} = \frac{\Delta V}{V_0}, \quad (1)$$

with V_0 being the initial volume, with no loading, of the considered material. In our case, this EOS will be made of three different parts, illustrated in figure 6.

- In the *elastic* part of the EOS, the pressure/deformation law is a straight line whose slope is the bulk modulus of the material, K_{el} .
- Above a certain pressure P_{el} , the material becomes plastic and enters the *pore-crushing* part of the EOS. It accumulates irreversible deformation. In the literature, this curve is known to follow an exponential law (see below).
- Finally, the pore-crushing curve crosses the *full-crush* part of the EOS. At this point, all the material pores have been crushed and it behaves elastically. The EOS is a straight line with a slope K_{fc} similar to the elastic bulk modulus of a rock made with the same compounds as the sand.

The HOSS user builds such an equation of state from scratch, in the form of the *EOS.input* file. In this file, the coordinates in (ε, P) of the three elastic, pore-crush and full-crush curves can be written, as well as the amount of tension (negative pressures) allowed for the material. It is thus possible to fix by hand the parameters P_{el} , K_{el} , and the properties of the pore-crush curve (exponent, initial slope) needed in the model. These parameters will describe one element, a tetrahedron containing several thousands of sand grains, of the simulation. To allow mesoscopic transport of the sand particles, no cohesion is set between these "sand elements", which are free to contact and rub each other with a certain friction coefficient, or fly away from the test bed into the ejecta.

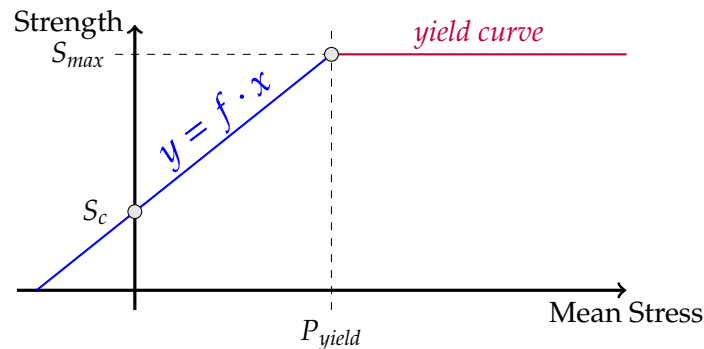


Figure 7 – Description of the typical Strength Model of a sand material

The deviatoric law, or Strength Model, describes the link between the deviatoric and mean stress applied on a volume. When the strength becomes too high, materials *yield* : they are damaged and can no longer resist to an applied stress. For each overall stress value, there is consequently a limit strength that cannot be exceeded. In continuum mechanics, this behaviour is portrayed with a *yield curve* as in Figure 7, with the mean-stress being the x- and the strength being the y-axis. As long as the material behaves in an elastic way, the yield curve is a simple straight line whose slope is the Mohr-Coulomb friction coefficient. The Strength value S_c of the yield curve at zero stress is called the *cohesion* of the material. When the mean-stress becomes too high though, this straight line flattens to become approximately horizontal or even decrease. This depicts how a material weakens under pressure, losing its initial frictional properties to behave more and more like a liquid. In HOSS, the *H7H.input* file allows the user to build a set of yield curves, for each direction and strain value. To find an appropriate model of pumice, all points of the curves can be modified, determining the parameters P_{yield} and the amount of friction. It is also possible to introduce anisotropy in the material response, and some *weakening* or *hardening* depending on the deformation.

Experimental studies of pumice sands at very high pressures and strain rates do not exist in the literature. However, many works on more classic sands can be found. These works give some insights on the variation of sand's properties with varying grain sizes, initial density, or strain

rates. For instance, as visible on figure 8, the initial density of a sand will highly influence its equation of state [Luo et al., 2011]. A sand with an initial density of 1.51 g/m^3 enters the plastic regime at lower pressure than a sand with an initial density of 1.75 g/m^3 , therefore a looser sand will also be weaker. The difference between a pumice sand and a regular silica sand is

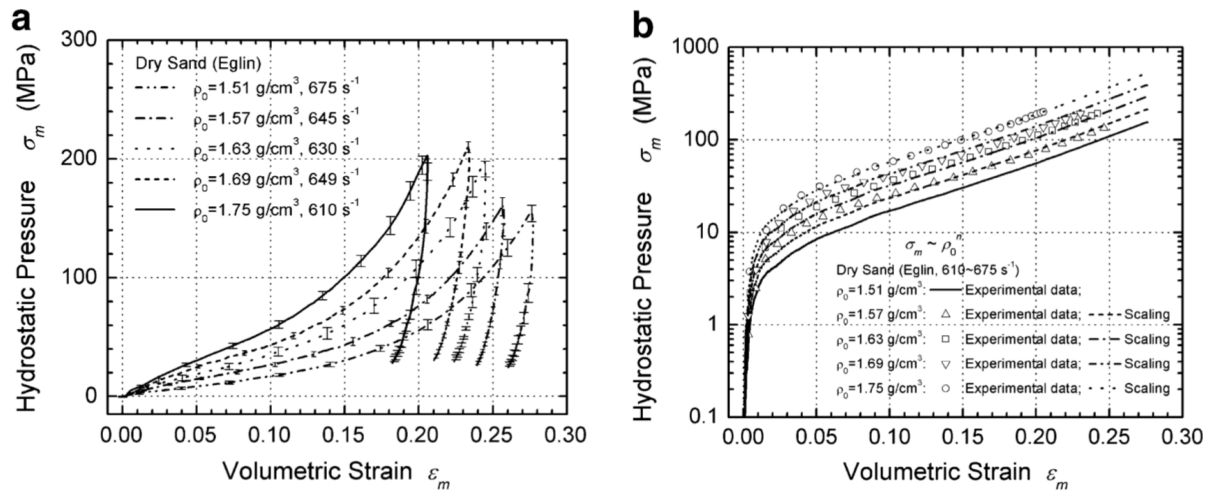


Figure 8 – Results of test of the hydrostatic pressure vs. volumetric strain of dry sand with varying initial densities. (a) Experimental plots, (b) plots calculated from the scaling law, in logarithmic scale. Reproduced from the works of [Luo et al., 2011]

hard to define without an appropriate experiment. One thing can however be deduced from the origin and formation of pumice sand. Pumice is a volcanic material formed by the cooling of a gas-rich lava. It is filled with gas bubbles, which produce many pores during the cooling process. Therefore, it can be assessed that a pumice sand will contain pores not only between grains, but also within the grains themselves. These supplementary pores make it a very low density material, and it can be deduced that pumice will be weaker and yield sooner than the sands of these experiments. And indeed, we know from the experimental description given to us by Drs. Richardson and Kedar that the pumice of the Martian runs weighs only 880 kg/m^3 instead of 1600 kg/m^3 for the sand of the Lunar runs.

2.1.5 Overview of the creation of the model

During the AVGR experiments, a pyrex or aluminium bolide hits some pumice sand. The aluminium and pyrex materials are well known from the literature and are well described by a Tillotson Equation of State [Tillotson, 1962] and a Von Mises yield criterion, which won't be discussed here. Without any literature on pumice however, it is not easy to assess its volumetric and deviatoric response. It makes it also very difficult to use generic equations of states of porous materials developed for shock codes, like the *snowplow*, the $p - \alpha$ or the $\varepsilon - \alpha$ models [Graham, 2012, Herrmann, 1969, Wünnemann et al., 2006, Collins et al., 2011]. Indeed, each of them requires a prior knowledge of some mechanical properties of the expected material, like its maximum elastic pressure or maximum elastic strain. We are left with only two informations: the density of the pumice, which is 880 kg/m^3 , and its porosity, which is 62%.

To overcome this lack of information, an alternative approach would be to conduct several systematic tests of the input parameters of HOSS, and empirically understanding their effects on the output shock wave. In particular, the effects of the two models *EOS.input* and *H7H.input* need to be understood. To do so, several tests were made on the typical parameters of these models: the yield pressure P_{yield} , the transition pressure P_{el} , but also the shapes of the pore-crush curves and bulk moduli.

Our tests had to be comparable to the typical size of the AVGR experiments. For this reason, their geometry was designed with the software *Cubit* so as to match the dimensions of the laboratory shots. A 30 degrees wedge representing the sand and the bead was set up, as visible on figure 9. To optimize computation time, sand elements sizes increased away from the impactor. The closest elements had a typical size of 1mm and thus contained around a thousand sand grains. The sand and impactor elements were kept in place by two fixed walls, that could only contact them and not exchange any energy with them. As said before, all sand elements were made cohesionless and independent from each other to mimic the transport of sand grains, but are described by the same material model. They interact by contact and friction. The modelled sand tank was provided with sensors every centimetres in the vertical direction and 45° from the impact point. To reduce the computing time, the first tests ranged only 30 to 50cm in depth and in radius. The final setup of figure 9 covered the entire dimension of the AVGR tank and avoided reflexions of the shock wave on the borders to interfere too soon with the desired signal. For simplicity, gravity was ignored in these tests. This results in a wrong approximation of the crater and ejecta shapes, but is not supposed to change the simulation outcomes as long as the hydrostatic pressure is smaller than the shock stresses.

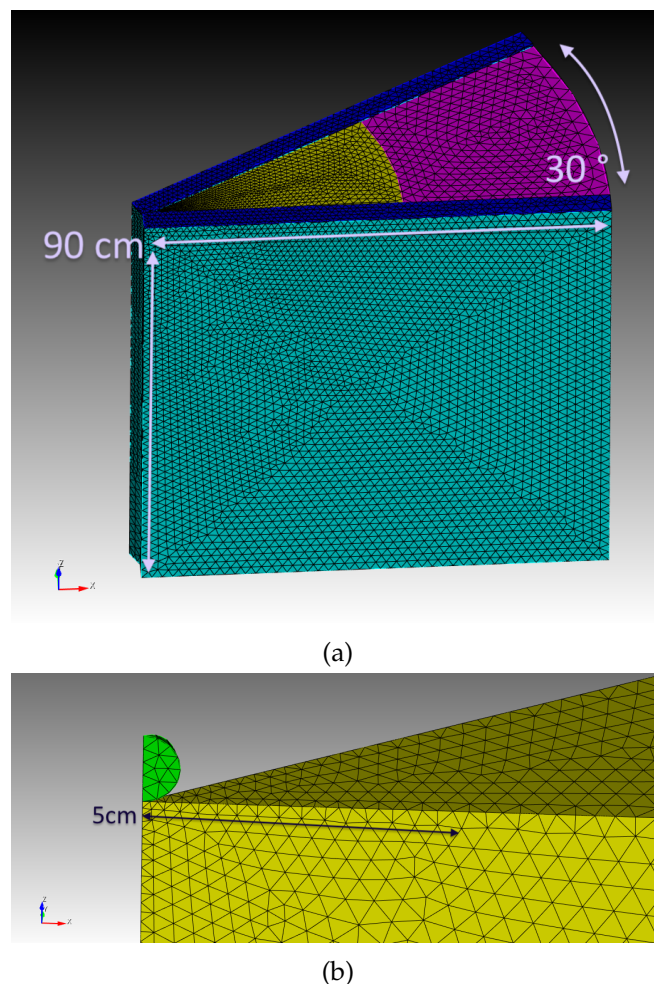


Figure 9 – Screenshot of the setup used for this project, rendered with the software *Cubit*. (a) shows a 30° wedge of sand (0 to 50cm in yellow and 50 to 90cm in pink) between two walls (blue and turquoise), meshed with ~ 375000 elements. (b) shows a zoom on the 30° pyrex or aluminium bead reproducing the AVGR impactor, in green.

As a start, the model of sand designed by researcher Zhou Lei from the HOSS developing team was used. This initial model is based on the works of [Luo et al., 2011, Berney et al., 2008] and

is reproduced on figure 10.

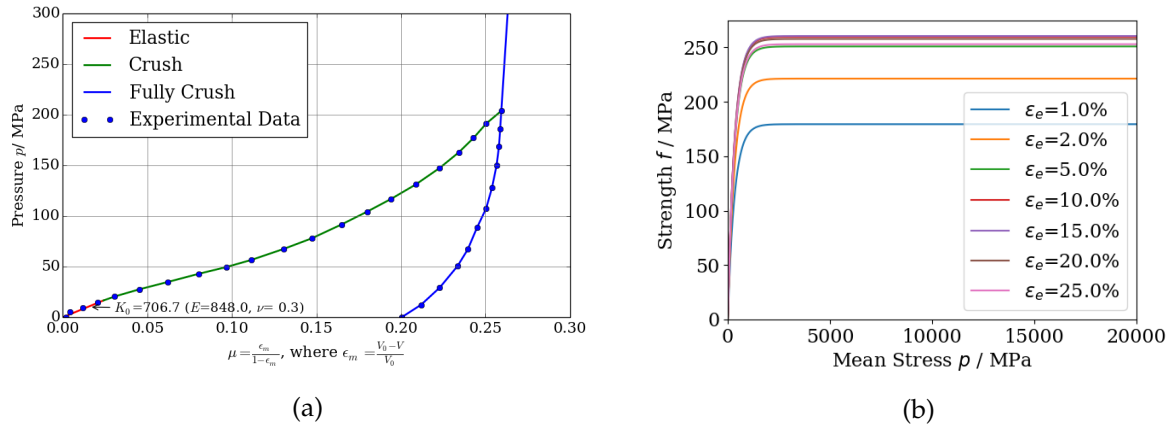


Figure 10 – Initial EOS (a) and Strength Model (b) used as a base for a pumice model. Reproduced from the work of Zhou Lei (2019, pers. comm.).

2.2 Tests on the EOS and H7H : presentation, results and analysis

2.2.1 The elastic properties of the experimental material

Our first tests aimed at investigating the influence of the elastic properties of our sand on the wave propagation. When the applied pressure drops below a certain level, the material volumetric behaviour is described solely by its bulk modulus. For instance, in the work of Luo et al. [2011], this bulk modulus and transition pressure were found to be $K = 700$ MPa and $P_{el} = 20$ MPa. The pressure wave velocity for an elastic medium is given by

$$c = \sqrt{\frac{K}{\rho}},$$

where ρ is the density of the medium. When this model was used in the first runs, it became very clear that the resulting propagation velocities for the pressure waves were too high. These tests aimed at changing the bulk modulus in the elastic domain and analyse the effect of this change on the wave propagation velocity. This study tried to reach for velocities closer to the one recorded in the AVGR experiments, that is to say 250 m/s in sand and 150 m/s in pumice.

Figure 11 shows the initial EOS and the two modified EOS that were used for this test. The legend box indicates the bulk moduli set for these three models. At this point in time, we had not communicated with the principal investigators of the experiments and ignored about any of the pumice characteristics. A generic sand density of 1700 kg/m^3 was thus used to deduce the wave speed. The sensors lined every 1cm in two directions made it possible to measure the wave arrival times and thus the velocity of the wave as it passed them. Figures 12a and 12b show the plots of these wave velocities with distance from the impact. Depending on the elastic bulk modulus, the shock wave velocity decreases and converges to the sound speed determined from the bulk modulus.

These first two tests confirmed the importance of the elastic behaviour of the sand in the late stages of the propagation. Despite our limited knowledge of the pumice sand's material properties, the study of the experimental seismic data gives some clues on its elastic response, allowing us to set the slope of the elastic part of the EOS curve. However, the boundaries of this elastic domain are yet to be assessed.

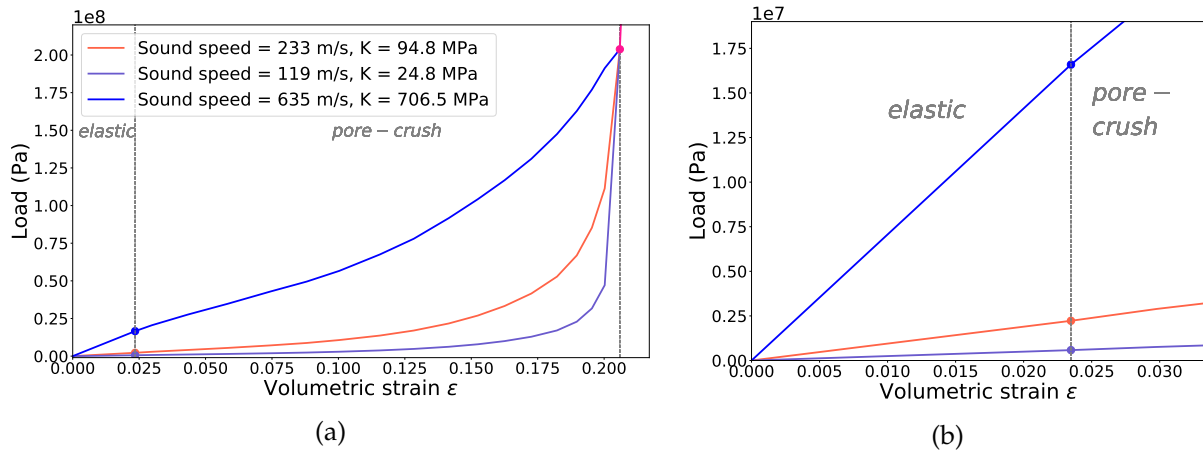


Figure 11 – Curve of the initial (purple) and modified EOS (blue and orange) (a) used to investigate the wave speed. (b) shows a closer image of the three different elastic domains.

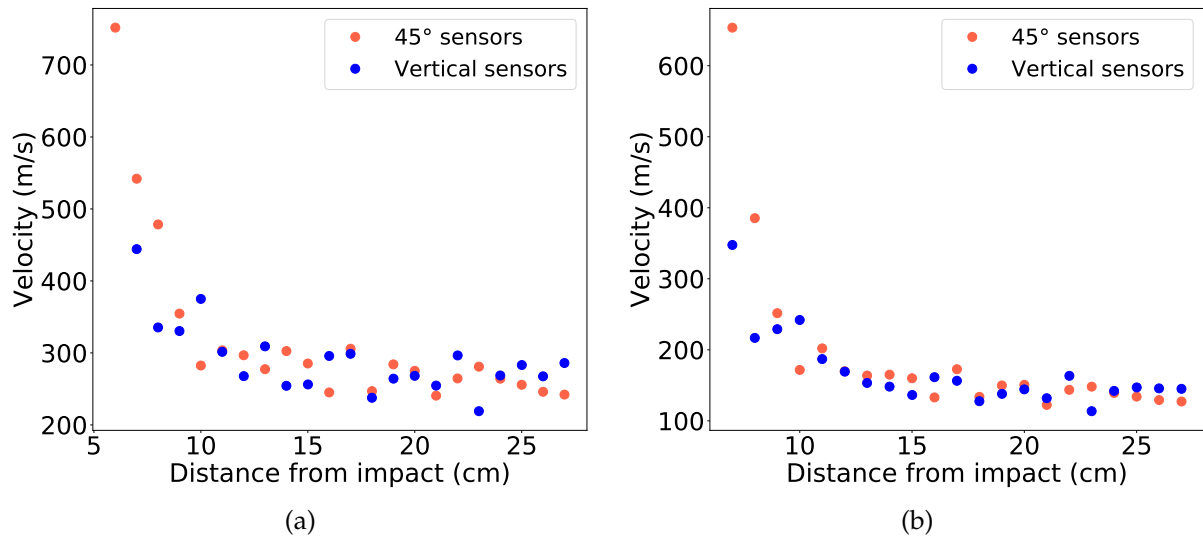


Figure 12 – Velocity of the shock wave associated to the EOS of figure 11, measured between two successive sensors for $K = 94.8$ MPa (a) and for $K = 24.4$ MPa (b).

2.2.2 Transition from the elastic to the plastic regime in the EOS

Following the study of the elastic domain of the volumetric equation of state, this work focused on the transition to the pore-crush domain. The partitioning of energy in impact phenomena is yet not well understood. However, this problem can be simplified by taking a first order look at a mesoscopic sand element.

As the shock wave crosses an element volume, the incoming energy will have two main roles. Part of it will generate a mechanical work proportional to the applied pressure and the elementary volume change, as $\delta W = -PdV$. The other part of it will generate dissipative processes in the form of temperature changes, phase transitions and, in our case, the plastic deformation and crushing of the material. HOSS' Equation Of State allows the user to establish the pressure response in function of the deformation ϵ , with ϵ being directly proportional to this element's volume change (see equation 1). Using an integration by part, it is found that :

$$\delta W = -P\epsilon V_0 = -V_0 \int (P + \frac{dP}{d\epsilon}\epsilon) d\epsilon. \quad (2)$$

From this, it can be understood that the area below the EOS curve is determining the mechanical work that the sand undergoes. The smaller this area is, the stronger plastic dissipation phenomena will be, given that the total available energy remains the same. It is thus expected that more energy will be dissipated inside the sand when the plastic pore-crush curve starts at lower pressures.

Therefore, another test was designed to investigate this transition pressure. Three EOS were constructed. As shown on Figure 13a, their curves were chosen so as to keep the same slope in the elastic regime, drawn here in blue. Then, a similar pore-crush law was designed, and shifted to intersect the elastic regime curve at three different transition pressures, P_{el} . The same sensor points as in section 2.2.1 were used to observe the shock wave. Figure 13b shows the peak pressure signals measured at each of these sensors. The three curves show that P_{el} indeed has an influence on the pressure decay with distance. More precisely, a transition between the elastic and the plastic regime can be observed for each of these tests. For $P_{el} = 10^5$ Pa and for $P_{el} = 10^4$ Pa, the pressure decay law changes slope once the pressure drops below the elastic limit, materialised on the figure by two plain lines.

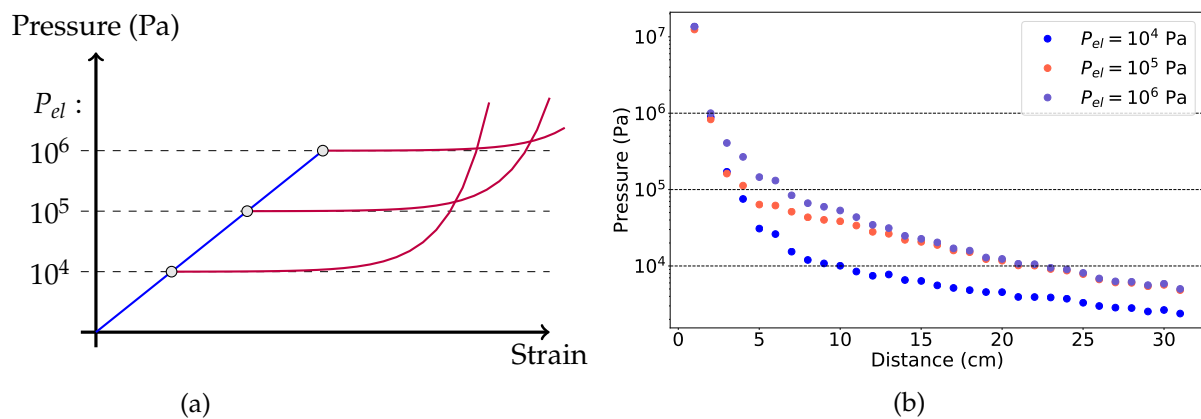


Figure 13 – (a) Graphic of the three EOS used to test several transition pressure (b) Peak-pressure decay with distance for these three transition pressures.

The transition between these two domains is even visible on a single sensor, if it stands close to the transition distance. Two examples are shown on Figure 14. The two plots show the pressure and velocity signals observed at a particular sensor in the case of $P_{el} = 10^5$ Pa (a) and $P_{el} = 10^4$ Pa (b). These sensors stand respectively at 5cm and 8cm from the impact, which means, according to figure 13b, that they are both experiencing pressures above P_{el} . And indeed, on the pressure signals themselves, the initiation of plastic deformation is visible : the wave jumps from one regime of propagation to the other at $P = P_{el}$, as shown by the dotted lines of figure 14.

This changeover creates a simultaneous bump in the velocity signal. In shock physics, this bump is called the *elastic precursor* and has interesting properties. It appears only when the transition from the elastic to the plastic domain creates a deflexion [Grady, 2017, p. 28]. This precursor is supersonic : the first arrival in 14a and 14b corresponds to a velocity of 250 m/s for $P_{el} = 10^5$ Pa and 200 m/s for $P_{el} = 10^4$ Pa. As shown by Figure 13b, it decays slower than the plastic wave following it. In fact, after the transition to the elastic domain, the elastic precursor is all that remains of the shock. Therefore, if the transition pressure is too high compared to the pressure applied on an element, no elastic precursor is visible, because no plastic wave is created.

The elastic precursor is a precious indicator of the failure threshold of materials. As will be shown later, some of the sensors of the AVGR experiments display two successive waves, very

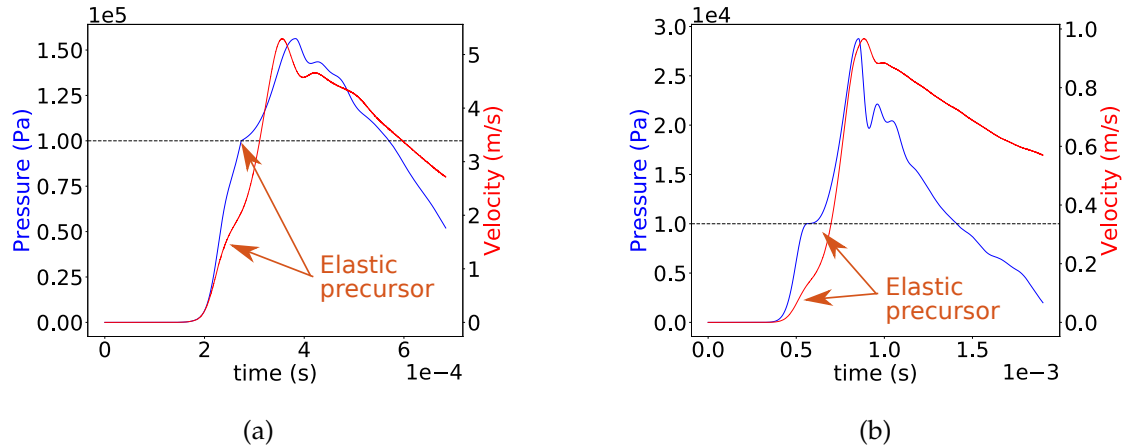


Figure 14 – ((a) shows the pressure and velocity (norm of the vector) waves associated to a transition at 10^5 Pa, seen at 5cm from the impact. (b) shows the same changeover for a transition at 10^4 Pa seen at 8cm from the impact.

similar to an elastic precursor and its plastic successor (see Appendix A). These tests can thus be used to constrain the pumice volumetric properties.

2.2.3 Transition from the elastic to the plastic regime in the Strength Model

The strength model is an important part of impact simulations. The deviatoric response of the material conditions the appearance of shear waves. It has importance for seismic detection as the partition between pressure and shear energy can be monitored by seismic observation. Therefore, its influence on the shock wave needs to be investigated.

To this end, a set of tests was designed. One particular EOS was chosen to solve the volumetric deformations, and four yield curves were chosen for the deviatoric model. These four yield curves are drawn on figure 15a. All of them show the same initial relationship between strength and mean stress, which is similar to a Mohr/Coulomb relationship with a friction coefficient of 0.7. This curve is shown in blue. However, above a certain stress, here called P_{yield} , the fracture curve switches to a horizontal line. This behaviour means that the material is allowed to yield. Because of the plasticity caused by the too high mean stress, a sand element cannot withstand more stress or friction, and acts like a viscous fluid.

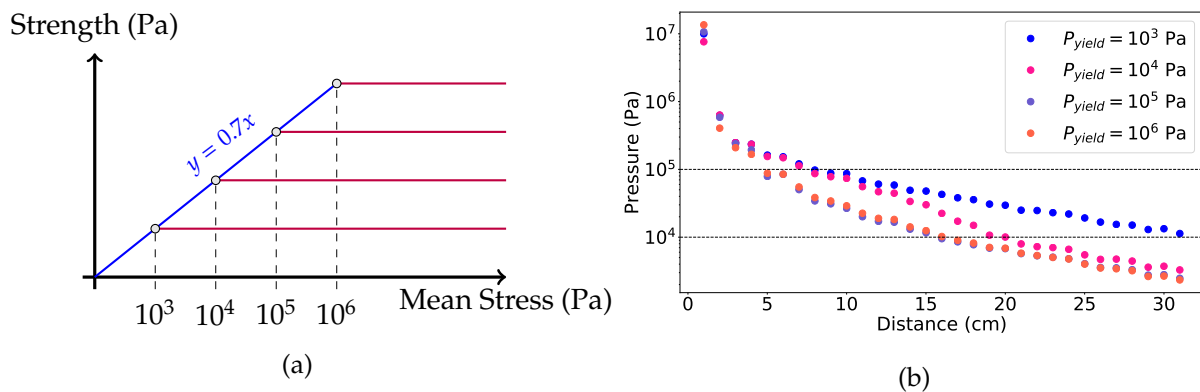


Figure 15 – (a) Four different strength models showing 4 different yield stresses. (b) Peak-pressure decay with distance found with HOSS for these strength models.

Once again, these four distinct models result in distinct decay features (see figure 15b). As said before, the energy partitioning of impact is still an active area of research, and the exact processes at play during yield remain unknown. According to this plot, the lower the yield stress, the higher the pressure amplitude. One interpretation for this is that, as the material yields, it becomes unable to dissipate as much energy as before through frictional processes. Instead of being dissipated, the remaining energy is used to further compress the considered element.

Once again, a transition between two regimes can be observed. When the pressure drops below 10^4 Pa, the curve of the model with $P_{yield} = 10^4$ Pa switches from a regime closer to the model with $P_{yield} = 10^3$ Pa to a regime closer to the two other models. After a distance of propagation of 20cm, it could be said that all of these three models follow a simple ideal Mohr-Coulomb law, setting a lower limit for the pressure decay law. The model with $P_{yield} = 10^3$ Pa is still yielding, and will join the other curves after more propagation, when its pressure drops below 10^3 Pa.

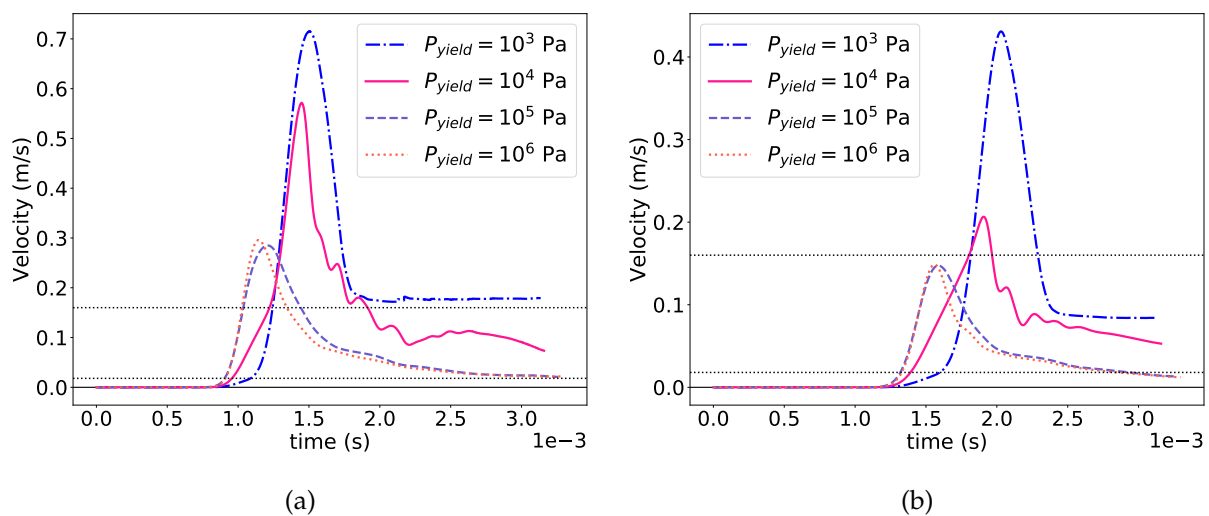


Figure 16 – (a) and (b) show the norm of the four velocity waves associated to four distinct yield stresses, seen at 16cm and 20cm from the impact respectively. The limit between the frictional and yield regime is marked with dotted lines for $P_{yield} = 10^3$ Pa and $P_{yield} = 10^4$ Pa.

The transition from yield to linear friction results in a visible feature on the sensors' time series. Figure 16a (resp. 16b) displays the velocity signals recorded at 16cm (resp. 21cm) for all four yield models. At these distances from the impact, the models with $P_{yield} = 10^5$ Pa and $P_{yield} = 10^6$ Pa have reached the linear friction regime, and indeed their signals are very similar. The model with $P_{yield} = 10^4$ Pa however, is still partly yielding. Below the dotted line, the velocity follows a slow, straight slope. The shock energy is still absorbed by friction. Above the dotted line, the velocity signal's slope becomes steeper and its amplitude is bigger than the two previous models'. This is a sign of the material's yielding. The energy, which cannot be consumed in plastic phenomena as much as before, goes in the element's kinetic energy. The same phenomena is visible for the model with $P_{yield} = 10^3$ Pa, even if the transition happens significantly sooner, as seen by the lower dotted line.

2.2.4 The plastic pore-crushing curve in the EOS

From equation 2, it can be inferred that $\frac{dP}{d\varepsilon}$, the derivative of the EOS, might have an influence on the wave amplitude. As shown in section 2.2.1, the slope of the EOS in the elastic domain is fixed by the wave velocity observed in the experiments. However, the slope of the pore-crush

curve is not yet constrained. In the litterature, experimental study of sands at high or low strain rates show that the plastic behavior of sand can be approximated by the law

$$\sigma = \sigma_0 + A_0 10^{m\varepsilon}, \quad (3)$$

with m between 4.5 and 5.5 and σ being a measure of stress similar to pressure [Luo et al., 2011, Yamamuro et al., 2011, 1996]. The following section presents the influence of a variation of the initial slope A_0 and of the power m on the observed pressure and velocity signals.

First, the influence of the coefficient A_0 at the beginning of the pore crush regime was investigated. Four EOS were designed, as seen on figure 17. Their pore crushing-law used the same parameter $m = 5$, but were shifted horizontally and vertically in order to have different slopes at $P = P_{el}$. The equivalent bulk modulus of these transitions was computed and is shown on figure 17.

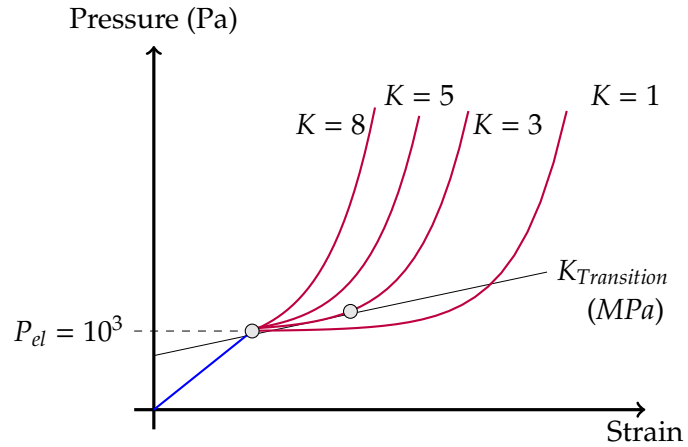


Figure 17 – Graphic of the four Equations of State used to test several transition slopes

The influence of the EOS' slope on the amplitude is demonstrated by figure 18a. The lower the initial slope, the lower the overall amplitude of the pressure wave. The difference in peak-pressure between the case $K = 8$ and $K = 1$ MPa is almost a decade. This tends to show that the derivative of the EOS has as much, if not more influence on the energy dissipation, than the area below the curve.

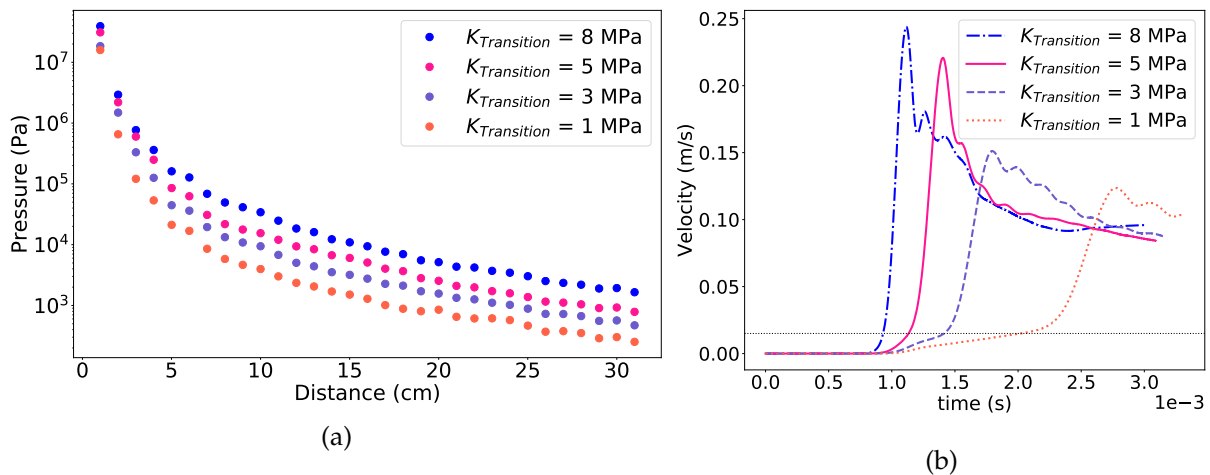


Figure 18 – (a) Pressure decay with distance for four distinct transition slopes. The approximate bulk modulus at the transition is taken lower than the bulk modulus of the elastic domain, which is 10 MPa. (b) shows the four associated velocity waves measured at 15cm from the impact.

In terms of velocity signal, the influence of this choice of curve is also strong. Figure 18b shows four velocity signals, recorded at 15cm from the impact point, for each of these volumetric

models. The pore-crush curve initial slope appears to have a significant influence on the elastic precursor shape and length. The lower the pore-crush slope is, the slower this precursor and the following wave are. This difference in arrival time and amplitude is useful to constrain the model with the experiments. Indeed, the duration of the elastic precursor, its arrival time, and the peak velocity time may all be measured on the experimental accelerometers. Using these informations, an appropriate value of K can be inferred by interpolation from our 4 test values.

If the initial slope of the pore-crush curve has such a big influence on the velocity signal, then what about the derivative at higher pressures? Given a fixed initial slope, the later parts of the curve might change significantly depending on the chosen exponent m . The influence of this parameter was investigated. To this end, four new EOS were built. This time, the initial slope was kept constant, but the exponent m was changed from 3 to 6 (see figure 19).

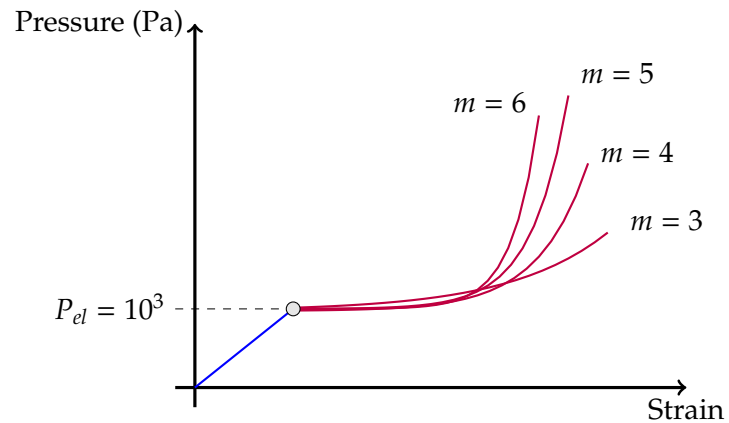


Figure 19 – Graphic of the four Equations of State used to test several exponents of the pore-crush curve

Results are shown on figure 20a and 20b. This time, it seems that the pressure decay is not significantly influenced by the change in the EOS slope at high pressures. Looking at the velocity signals, it seems that the elastic precursors have roughly the same duration. The peak velocity seems to be the same. One simple explanation for this is that, during propagation, only the elements closest to the impact will be submitted to very high pressures. At longer distances, the pressure drops quickly below 10^4 Pa. Hence, at low pressures, all exponential curves look the same and have the same slope. The difference between them is only visible at extreme strains and stresses.

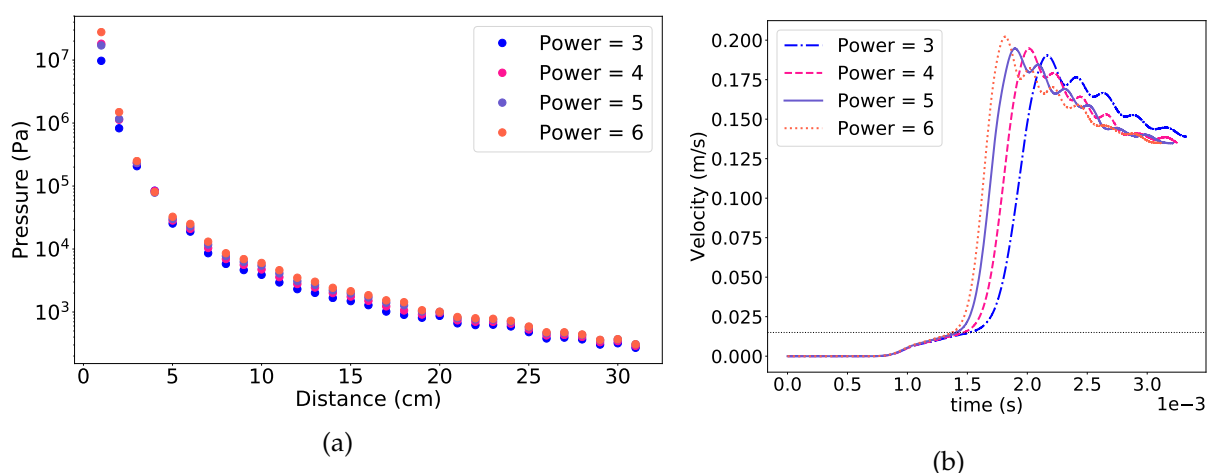


Figure 20 – (a) Pressure decay with distance for four distinct powers of the pore-crush curve. (b) shows the four associated velocity waves measured at 13cm from the impact.

It can thus be deduced from this test that experimental results will only allow to constrain a model of limited pressures and strains. Looking at the elastic precursor and the peak velocity and acceleration, it will be possible to constrain the beginning of the pore-crushing curve, but its

later stages will not be accessible. It will be necessary to make hypothesis, based on literature, on the power m of the curve.

2.2.5 Equation of state for extreme strains and stresses

As said before, little can be known on the material properties at extreme strains and strain rates. From the porosity, a maximal theoretical strain can be computed. The porosity α is defined as the ratio between the pore volume V_s and the total volume V of an element. When this element has been fully crushed, which means it does not contain any more pores, it should have been affected by a loss of volume V_s . Thus, the maximal strain of a fully-crushed material is theoretically:

$$\epsilon_m = \frac{\Delta V}{V} = \frac{V_s}{V} = \alpha. \quad (4)$$

In reality, a fully crushed material can still sustain deformation. Indeed, the remaining non-porous material will act itself as an elastic solid, and deform even more under pressure. This solid, though, should be far more stiffer than the initial material. This reasoning was made by [Güldemeister and Wünnemann, 2017] in their simulation of porosity in hypervelocity impacts. In their work, solids with no porosity were represented by rocks made of the same minerals. Hence, different kinds of tuff with different porosities were compared to a perfect quartzite cristal. The speed of sound and density in such crystals are known. For quartzite, [Güldemeister and Wünnemann, 2017] used a 5000 m/s sound velocity, which results in a bulk modulus of $K \sim 60$ GPa.

During our tests, the full-crush curve (see Figure 6) was occasionally modified to correspond to different porosities. But the full-crush curve connects with the pore-crush curve only at pressures higher than 10^8 Pa. In the case of such a small impact, only very few elements close to the impactor reach this curve. A larger distances, the full-crush curve has no influence on the observed outputs. Therefore, it is not possible to constrain this part of the curve with the experimental data.

2.3 Creation of the regolith model

2.3.1 Interpretation of the tests

Parameter	Effect on wave velocity	Effect on amplitude	Effect on elastic precursor
K_{el}	deciding factor at long distances	small	precursor exists if $K_{trans} < K_{el}$
P_{el}	small	important	determines distance at which precursor disappears
P_{yield}	small	important	negligible
K_{trans}	important at the plastic-elastic transition	very important	very important
m	important at small distances	negligible	negligible

Table 2 – Summary of the effects of each studied parameter.

Following the set of tests from section 2.2, inferring some parameters for a pumice model was made possible. To do so, observation made on the experiments and the previous results were combined. The table of figure 2 sums up all the effects of the previously studied parameters.

What follows is the discussion that led to a certain choice of parameters for the model. The observations allowed by the experimental data are summarised in Appendix A. The final parameters are summarised in table 3.

The elastic bulk modulus K_{el} For both Shot #22 and Shot #13, the travel time of the acceleration and velocity wave between the vertical sensors of the AVGR experiments gives the same P-wave velocities of around 150 m/s. By implication, with a density of 880 kg/m³, the value of K_{el} was found to be 10 MPa.

The transition Pressure P_{el} The elastic precursor is visible on the acceleration signal of the vertical sensors of Shot #22 and Shot #13. However, the tests showed that in most cases, geometric attenuation of the wave results in pressures lower than 10⁴ Pa at 21cm from the point of impact (see 18a, 20a). Therefore, the fact that the transition from the elastic regime to the plastic regime is visible at 21cm from the impact point means that this transition occurs at pressures lower than 10⁴ Pa: $P_{el} \leq 10^4$ Pa. By using a few values between 10³ Pa and 10⁴ Pa, it was found that $P_{el} = 10^3$ was best fitting the elastic precursor of the vertical sensors at 21cm and 42cm for Shot #13.

The transition slope K_{trans} of the pore-crush curve The experiments give use the amplitude and peak time of the velocity and acceleration waves at several sensors. It has been proven that the transition bulk modulus K_{trans} has a strong influence on both these values. Using a set of slopes similar to Figure 17, it is possible to get velocity and acceleration signals similar to Figure 18 at 21cm and 42cm vertically from the impact. By interpolation, a value of K_{trans} that yield the right amplitude and peak time can be inferred. The value of $K_{trans} = 6$ MPa was best fitting the experimental signal.

The power m of the pore-crush curve This parameter was proven to have a limited influence on the wave's shape at long distances, given the fact that most of the wave measured at the experimental sensors is in the elastic regime. The value of $m = 5$ was chosen, which was the mean value of the power found in high-pressure, high-strain rate laboratory experiments on sand in the litterature [Luo et al., 2011, Yamamuro et al., 2011, 1996].

The full-crush curve The same argument as for the previous parameters leads us to say that this full-crush curve will have a limited influence on the signals measured at the sensors. For the sake of consistency with literature and especially the works of Gldemeister and Wnnemann [2017], the full-crush curve was considered similar to the elastic bulk modulus of a quartzite.

The yield value P_{yield} As seen in section 2.2.3, a low yield pressure can result in artifacts in the signal's shape and amplitude. There is no indication of such a behaviour in the experimental signal. Therefore, the hypothesis was made that the yield pressure was higher than the pressures reached in the experiments and set it at $P_{yield} = 10^6$ Pa.

K_{el}	P_{el}	P_{yield}	K_{trans}	m	K_{fc}
10 MPa	1 kPa	1 MPa	6 MPa	5	60 GPa

Table 3 – Final parameters for the pumice model.

2.3.2 Comparison of the obtained model with the experiments

With these parameters, a comparison between experimental signals for Shot #13 and signals produced by HOSS with the previously defined model, is visible on figure 21. Given the very

long computation time necessary for such model (~ 100 hours), only the closest sensors at 21cm, 30cm and 42cm are shown.

HOSS signal show good arrival times for vertical sensors at 21cm and 42cm. Peak negative velocity are similar to the experimental values of -7 cm/s and -1.2 cm/s. For the horizontal sensor at 30cm, the peak vertical velocity matches the experimental results at 3 mm/s, and the peak radial velocity is 9 cm/s instead of 6 cm/s. In the acceleration signals, the elastic precursors appear at the right time for the vertical sensors, although they have a slightly bigger amplitude.

All the parametric tests conducted in the previous sections on the pumice response (except the tests on the K_{el} parameter) were made with the impact velocity of Shot #13, which is 980 m/s. Indeed, the high impact velocity of 5820 m/s in Shot #22 caused this setup to be unstable and made it more difficult to get reasonable computing times. However, once the pumice model was tuned for Shot #13, it became possible to apply it to Shot #22. Figure 22 shows the velocity and acceleration waves obtained 21cm down the impact point with an aluminium impactor and a shot velocity of 5.82 km/s. Despite the factor 5 difference in impact velocity, the experimental and numerical signals amplitudes are not too far from each other in Shot #22. The peak negative acceleration is $-2.5 \cdot 10^3$ m/s² for HOSS's signals and $-4.5 \cdot 10^3$ m/s² for the accelerometer, which corresponds to 40%. In velocity, this difference is only 15% (from 0.5 to 0.58 m/s). The weak elastic precursor arrival time in the numerical acceleration signal is 0.8 ms, like in the experiments.

2.4 Limitations of our study

2.4.1 Discrepancies between the model and the experiments

As shown by the figures of section 2.3.2, the proposed pumice model also shows some defects and shortcomings. Even though the arrival time at the vertical sensors show a good agreement with the Shot #13 and Shot #22 experiment, it is not the case for the horizontal sensors, whose numerical signals have to be shifted to match the experimental ones. In the horizontal direction, the arrival times and shock durations produced by the numerical simulation are too short (2 ms instead of 4 ms). The model misses the complexity of the observed waves, whose velocity is slower than the vertical pressure waves. As surface waves depend more strongly on the deviatoric response of the sand, this tends to indicate that our Strength Model needs to be modified.

Furthermore, a discrepancy between the elastic precursor of the closest sensor of Shot #22 and the numerical model can be noticed. The shape of the elastic precursor produced by HOSS for Shot #13 is in agreement with the experiments, but this is not the case for Shot #22. An amplitude of $-4.5 \cdot 10^3$ m/s², similar to the plastic wave, is measured in the experimental signal. But the elastic precursor is weak ($< 1 \cdot 10^2$ m/s²) in the numerical signal. Unfortunately, given the instability resulting from the high strain rates of Shot #22 and the computation time needed to simulate it, this study had to focus on Shot #13. This disagreement might thus be explained by the high-pressure pore-crush curve, which is hard to constrain with the lower velocity experiment as the pressure reached in the pumice are smaller. A too weak numerical wave could indeed indicate that our pore-crush curve is not steep enough at high pressure, and that the power of the curve should consequently be higher than $m = 5$. A future work should focus on Shot #22, to investigate the high-pressure EOS and its effect on the arrival times.

In the same way, a spurious flattening of the velocity wave is visible on all three sensors for Shot #13, at 5ms for 21cm, 4ms for 42cm and 3ms for 30cm. As will be discussed later, this flattening could have several explanations. For the horizontal sensors, it might be caused by the absence

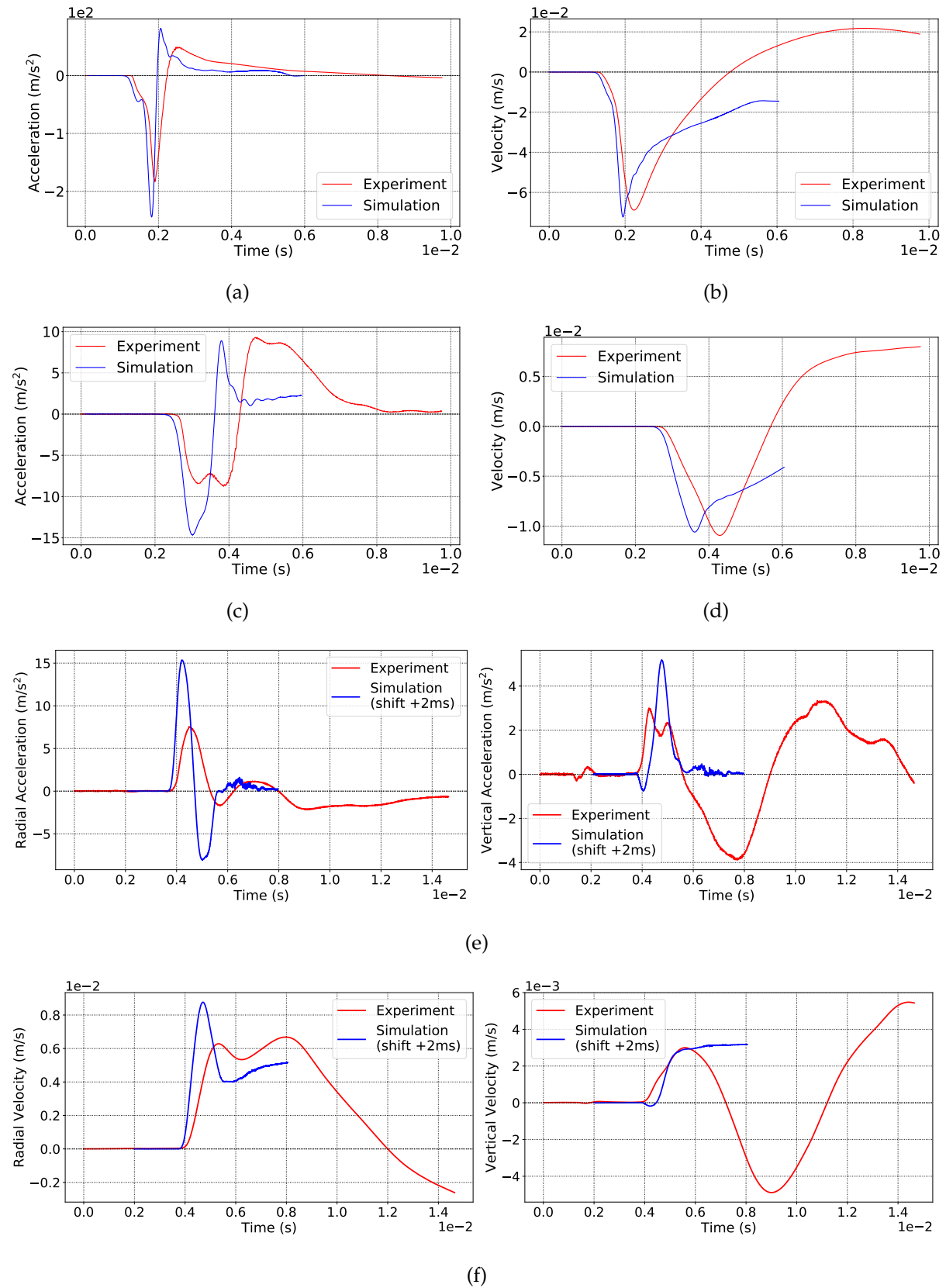


Figure 21 – Comparison of the experimental and numerical acceleration and vertical velocity signals obtained with Shot #13 at 21cm vertically from the impact (a and b in the vertical direction), 42cm vertically from the impact (c and d in the vertical direction) and 30cm horizontally from the impact (e and f in the vertical and radial direction, simulation time shifted by 2ms.)

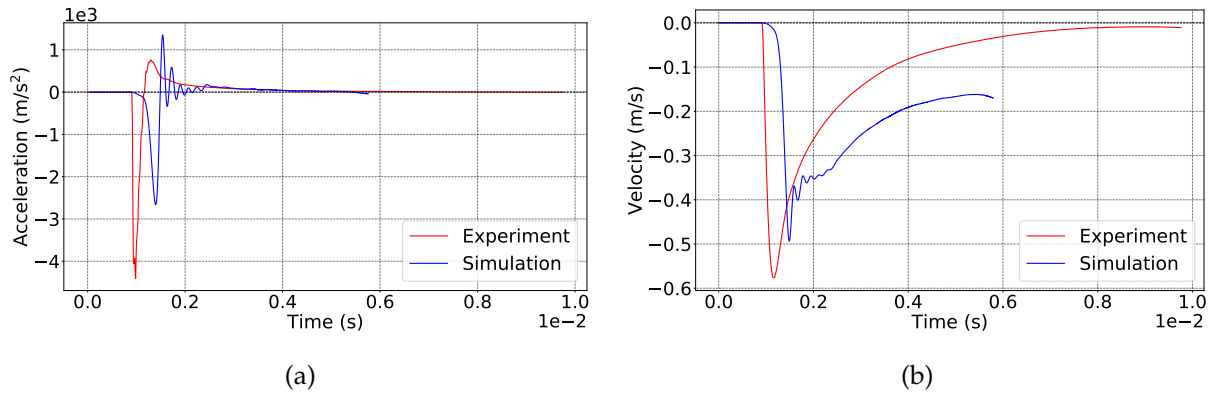


Figure 22 – Comparison of the experimental and numerical vertical acceleration (a) and vertical velocity signals (b) obtained with Shot #22 at 21cm vertically from the impact.

of gravity in the model. However, for the vertical sensors, no explanation has yet been found. It should be pointed out that this velocity flattening depends on the material model, as shown for instance by the yield pressure tests of Figure 16a and 16b. During these tests, a constant velocity was left after the passage of the shock, whose value seems to depend on P_{yield} .

Finally, our numerical model struggles at representing the velocity *rebound* observed in the experiments. Indeed, the experimental signals integrated from the acceleration clearly show the velocity taking positive values (at 4.8 ms for the Z-velocity at 21cm) and oscillating around zero as the shock dissipates. This behaviour is not well reproduced by our simulation. This absence of rebound could have several explanations, some of them are related to the “spurious flattening” discussed before. One is linked to an hypothesis made very soon in this work, which is the absence of *tension* in the sand. Due to the granular nature of sand, it was considered unable to resist to positive pressures (negative pressures being compression in our convention) in its volumetric or deviatoric response. This hypothesis might need to be investigated, as tension could be the cause of this upward bounce, like with a metallic spring hitting the ground, .

2.4.2 Future investigations on the experiments

In addition to the three limitations previously addressed, many other parameters of the model might have an influence on the result and should be thoroughly investigated. The following section proposes possible future works on the pumice setup.

- First of all, the experimental data have not been fully used in this study. To completely validate this representation of a pumice sand, the movies and crater measurements provided by Drs. Richardson and Kedar would need to be compared to the numerical results. More precisely, HOSS simulations would need to be pushed further in time to get a crater profile and size, and the ejecta angle over time. These informations are present in the movies and data gathered during the 2012 AVGR campaign. However, this task comes at a very high computing cost : crater formation takes around 100ms and would requires a few weeks of computation with the present HOSS setup. A future work could consist in building a rougher mesh, to be able to investigate the crater shape over a longer time.
- Gravity was ignored in this work. Indeed, according to the works of Holsapple [1987, 1993], on Earth, gravity will start to be a constraint for crater shapes only for impactors larger than a meter. Nevertheless, this parameter might be of some importance to the shock wave itself, and could be investigated. In particular, we suspect gravity to cause several spurious effects on our simulations, like for the signal of the sensor at

30cm from the impact point. This sensor is buried 6cm deep into the sand, it is thus very close to the surface of the testbed. As seen on figure 21f, its velocity signal shows strange characteristics : after the wavefront passes the sensor, both the radial and vertical numerical velocities stabilise at a constant positive value, instead of oscillating around zero like in the experiments. The experimental velocity decreases by 8mm/s in only 3ms, which corresponds to an acceleration of 2.6m/s^2 . This value is of the same order of magnitude as the terrestrial gravity. It indicates that gravity could be the cause for this downward acceleration. The flat velocity of our numerical elements would simply be them flying up, instead of being pushed down by gravity.

Moreover, in the depth of the sand tank, gravity may also have non negligible effects, some of which are the creation of *force-chains* under loading. These effects were investigated by Sun et al. [2009]. Due to the granular nature of sand, stresses do not distribute homogeneously inside a macroscopic volume of sand. Contact between sand grains being imperfect at the microscopic scale, stress tends to create chains linking a dozen of sand grain together. The hydrostatic pressure created by gravity could induce such force-chains to appear. The sand at depth would be pre-constrained and, according to Coulomb's law, would have a bigger strength and be harder to move around. This effect causes an exponential increase of wave velocities with depth. Morgan et al. [2018, Fig 10] showed that P-wave velocities could go from 80m/s at the surface to 160m/s at 1 meter depth because of *confining pressure*. This is similar to the velocity difference observed between the experimental horizontal and vertical sensors. The absence of gravity in our simulation might cause our sand particles to be under-constrained due to the absence of strong contact between the particles. This results in a so-called *fairy-castle structure*, observed for instance on the moon surface.

- Similarly, the effect of tension and cohesion in the sand is not fully understood. This study made the assumption of a completely unconsolidated, cohesionless sand that couldn't sustain any tension. What would be the effect of adding some cohesion between elements in the strength model? This could be done for instance by shifting damage curves to negative mean stresses, herewith allowing for a non zero strength at zero mean stress. An effect on the amplitude can be anticipated, because a more important part of the incoming energy might be transferred into deviatoric stresses. However, it is more difficult to anticipate its effect on the shock waves' shape.
- A well known challenge of numerical models concerns the mesh geometry itself. In the scientific community, modelers know that a regular, random mesh is necessary to get correct results. In particular, Pierazzo et al. [2008] has shown that a minimum number of 10 element per projectile radius (cppr) should be respected to get the right shock pressure values. Our models used a smaller cppr of 3. Moreover, our sand mesh elements are designed to represent a mesoscopic volume of sand. Given the sand grain size used in the AVGR tank (0.1 to 0.2mm), the elements closest to the bolide, whose typical size is 1mm, may contain more than a thousand sand grains. The furthest ones, whose length is closer to 2cm, will contain more than 8 million grains of sand. This mesh effect needs to be tested in a future work.
- One limitation of Lagrangian shock codes is that they are prone to stability problems, when some elements undergo too much deformation. The integration scheme used in HOSS becomes unable to resolve state values' evolution over a too short distance. The classical solution to this is simply to decrease the integration time-step, but this may cause a strong increase in the computation time. HOSS developers came up with another solution, which is a *stabilizer* algorithm. This stabilizer detects all elements that have exceeded a limit strain value, and artificially increases their stiffness. The involved element should stop deforming and avoid crashing the simulation. As far as this method only implies a limited number of elements, the resulting shock wave should be unchanged. However,

it could impact the estimation of the crater size, the crater elements appearing bigger than they should be. A sensitivity test of the stabilization process might be necessary in the future.

- The accelerometer used in the experiments have a finite dimension and weight. They are miniature Endevco 2256A-10 sensors similar in dimension to a cube of 1cm and weight 4.3gm. Their density is thus around 4.3g/cm^3 , to be compared to the 0.8g/cm^3 of the sand elements. According to its documentation, this captor has a flat response in frequency between 1Hz and 10 000Hz. But the effects of its shape and weight might still need to be investigated.
- Finally, this model has only been constrained with two available extreme sets of experimental data, which are Shot #13 and Shot #22. Is it valid for impact speeds inbetween 0.9 and 5.2 km/s (Shots #14, #20, #21) and for lower impact angles (Shots #15, #16, #17, #18, #19)? Could the conclusions of section 2.2 been applied to describe the 11 other tests targeting a sand bed instead of a pumice sand ? After all previous questions will have been answered, the study of these other AVGR tests would allow us to fine-tune our pumice model, and to develop another model of sand to widen our description of regolith.

2.4.3 Implications for a Mars-scaled impact

Some additional thoughts will here be discussed, concerning the implications of these results on the large-scale shock waves created by impacts on planetary surfaces. The goal of this work is indeed to create a model of Martian Regolith, fit to describe the typical material covering the surface of the planet. It is worth considering to what extent the pumice sand experiments really reproduce a planetary impact.

The pumice sand used in the AVGR "Martian atmosphere" tests are similar to the Johnson Space Center (JSC) Mars-1 Regolith Simulant [Allen et al., 1997] as said in section 2.1.3. However, even though this material might be similar in porosity and density to Martian near-surface dust, it might not be able to fully describe regolith. Indeed, this term incorporates a wide range of soils, including small stones and blocky ejecta. Though they are "unconsolidated" materials as well, they might show very distinct mechanical responses to impacts. For this reason, the modelling of more complex planetary soils will be necessary in the future. This internship paves the way to the construction of a two-layer model of the Martian surface, also including a bedrock layer at depth. Including this second feature will shed some light on the interaction between the shock wave and some harder, more cohesive materials below the soft regolith.

Moreover, the experiments were conducted with velocities ranging from 1 to 6 km/s. The minimum impact velocity on a planet is its escape velocity : 5km/s on Mars and 2km/s on the Moon. The impact velocity distributions computed for the Moon and Mars from observed asteroid populations yield a mean impact velocity of 9.6 km/s on Mars and 16.1 km/s on the Moon [Ivanov, 2001]. Therefore, the velocities reached in these experiment might be too small to fully constrain the impact processes at play on a planet. In particular, some of the information on the high-pressure response of regolith materials is missed in this study, as it has already been shown with the example of Shot #13.

Finally, it might be interesting to ask whether the Martian atmosphere might have an influence on impact processes as well. The AVGR movies showed that the tank near vacuum was still sufficiently dense to create some turbulences in the dust raised by the impact. Also, on the data of the two shots, some particular, low amplitude and very fast waves ($v \sim 600\text{m/s}$) could be observed just before the arrival of the shock wave, close to the surface. These shocks are thought to be *head waves*, which are triggered in the ground by the passage of a faster wave in the atmosphere. On Mars, the very low temperatures would result in a lower sound speed in

the atmosphere, but it could still have some effects on the propagation of seismic signals via a mechanical coupling between the atmosphere and the surface. All of these features of planetary environments might need to be investigated in future works.

3 Conclusion

During this internship, a numerical setup reproducing NASA/AVGR laboratory hypervelocity impacts of a bead on a pumice sand bed was built with the software HOSS. Using the same properties as these experiments, this numerical setup was used to find the parameters of the equation of state and the strength equation determining the response of the impacted pumice sand. To do so, the influence of six parameters was tested via six parametric studies.

These parametric studies showed that the elastic domain of the deviatoric and volumetric models had a strong influence on the shock wave produced by HOSS. In particular, the elastic bulk modulus K_{el} fixes the wave speed away from the source. They also showed that the transition from the elastic to the plastic domain was the cause of several features in the shock wave, like the elastic precursor. The latter is mostly determined by the transition pressure P_{el} and the transition slope K_{trans} in the equation of state.

The results of this study, combined with the characteristics of the observed experimental signal, allowed for the determination of a set of parameters for the pumice model. In particular, this model proved to fit the data of the vertical sensors, in terms of amplitude and arrival times. However, the model could not fit the wave arrival times of the horizontal sensors found in the experiments, and the upward velocities of vertical sensors.

These discrepancies call for further investigations, notably of the effect of gravity, stabilization and tension in the material model. A future model should also better include the data of the experimental Shot #22 to constrain the high-pressure response of the pumice sand, so that it could qualify to fit the extreme events of planetary impacts on regolith at higher scales.

To conclude, this internship was of great use to better understand the physical meaning of the parameters in the HOSS material model. Future works should answer the remaining issues of this pumice sand model, enabling potential use to model more realistic planetary soils, that include a bedrock layer below an absorbing regolith layer. Starting October, a new nine-months internship at LANL will initiate, using the same tool and models, a work on the yet unexplored effect of a low-density atmosphere on the seismic source of Martian impacts.

4 Acknowledgments

I wish to offer my sincere thanks to my supervising team. To Carene, who knew how to guide me in the big machine of LANL and shared with me, the newcomer, her knowledge of the American culture. To Esteban, who trusted me with the use of HOSS and the clusters, and spent so much time discussing with me every bump and curl of our shock wave. To Taichi, in IPGP, who helped me cross the bridge from impact simulation and geomechanics to seismology, even if we ran out of time to explore fully the link between all of these disciplines. Finally, to Philippe, who gave me the opportunity to do this amazing internship across two countries, supported my travel, and invited me to the InSight Science Team meeting, offering me a fantastic introduction to planetology. I am glad this collaboration will continue, deepening our understanding of impact seismology and supporting the exploration of Mars.

I would also like to thank Bryan and Alex (Zhou Lei) for their constant support during my time in Los Alamos. Bryan, for its infinite patience as I was constantly seeking his help while

learning to handle HOSS. And Alex, for his courses on numerical modelling and his help in the design of our model.

These words are also for Marina, whose path crossed mine in Los Alamos and who showed me New Mexico during our wonderful road trip. For Alex (Mazza) and Alex (McSpaden), Deborah, Soyoun, David, Hyosub, Jeremie, Garrett, who offered me some quality climbing sessions, and for Jessica and Tom who were very nice roommates. My arrival at the PSS team of IPGP also came with new faces and a new ambiance, and I am very thankful for the good time we had. Thank you Sabrina for your support in hard times. I hope I will be able to return all this help. Thanks Greg, Clement, Claudine, Sebastien, Philippe, Salma, Alice, Chloé, and everyone for these nice lunch breaks. I hope to be able to win even more at the "terrible riddle" contest.

References

- Carlton C Allen, Richard V Morris, David J Lindstrom, MM Lindstrom, and JP Lockwood. JSC Mars-1-Martian regolith simulant. In *Lunar and Planetary Science Conference*, volume 28, 1997.
- I.V. Berney, S. Ernest, and Donald M. Smith. Mechanical and Physical Properties of ASTM C33 Sand. Technical report, US Army Engineer Research and Development Center, Geotechnical and Structures Laboratory, 2008.
- GS Collins, HJ Melosh, and K Wünnemann. Improvements to the P- α porous compaction model for simulating impacts into high-porosity solar system objects. *International Journal of Impact Engineering*, 38(6):434–439, 2011.
- JEP Connerney, MH Acuna, PJ Wasilewski, G Kletetschka, NF Ness, H Reme, RP Lin, and DL Mitchell. The global magnetic field of Mars and implications for crustal evolution. *Geophysical Research Letters*, 28(21):4015–4018, 2001.
- I. Daubar, P. Lognonné, N.A. Teanby, K. Miljkovic, J. Stevanović, J. Vaubaillon, B. Kenda, T. Kawamura, J. Clinton, A. Lucas, et al. Impact-seismic investigations of the InSight mission. *Space Science Reviews*, 214(8):132, 2018.
- Ingrid J Daubar, C Atwood-Stone, S Byrne, AS McEwen, and PS Russell. The morphology of small fresh craters on Mars and the Moon. *Journal of Geophysical Research: Planets*, 119(12):2620–2639, 2014.
- Dennis Grady. *Physics of Shock and Impact*, volume 1. IOP Publishing, 2017.
- Robert Albert Graham. *Solids under high-pressure shock compression: mechanics, physics, and chemistry*. Springer Science & Business Media, 2012.
- Nicole Guldemeister and Kai Wünnemann. Quantitative analysis of impact-induced seismic signals by numerical modeling. *Icarus*, 296:15 – 27, 2017.
- W Herrmann. Constitutive equation for the dynamic compaction of ductile porous materials. *Journal of applied physics*, 40(6):2490–2499, 1969.
- Keith A. Holsapple. The scaling of impact phenomena. *International Journal of Impact Engineering*, 5(1-4):343–355, 1987.
- Keith A. Holsapple. The scaling of impact processes in planetary sciences. *Annual review of earth and planetary sciences*, 21(1):333–373, 1993.
- Boris A Ivanov. Mars/Moon cratering rate ratio estimates. *Space Science Reviews*, 96(1-4):87–104, 2001.

- P. Lognonné, W.B. Banerdt, D. Giardini, W.T. Pike, U. Christensen, P. Laudet, S. de Raucourt, P. Zweifel, S. Calcutt, M. Bierwirth, et al. SEIS: Insight's Seismic Experiment for Internal Structure of Mars. *Space Science Reviews*, 215(1):12, 2019.
- Huiyang Luo, Hongbing Lu, William L. Cooper, and R. Komanduri. Effect of mass density on the compressive behavior of dry sand under confinement at high strain rates. *Experimental mechanics*, 51(9):1499–1510, 2011.
- Arthur McGarr, Gary V Latham, and Donald E Gault. Meteoroid impacts as sources of seismicity on the moon. *Journal of Geophysical Research*, 74(25):5981–5994, 1969.
- Jay Melosh. *Impact Cratering: A Geologic Process*, volume 11. 02 1989.
- Paul Morgan, Matthias Grott, Brigitte Knapmeyer-Endrun, Matt Golombek, Pierre Delage, Philippe Lognonné, Sylvain Piqueux, Ingrid Daubar, Naomi Murdoch, Constantinos Charalambous, et al. A pre-landing assessment of regolith properties at the InSight landing site. *Space Science Reviews*, 214(6):104, 2018.
- Antonio Munjiza, Earl E. Knight, and Esteban Rougier. *Large Strain Finite Element Method: A Practical Course*. John Wiley & Sons, 2014.
- E. Pierazzo, N. Artemieva, E. Asphaug, E. C. Baldwin, J. Cazamias, R. Coker, G. S. Collins, D. A. Crawford, T. Davison, D. Elbeshausen, K. A. Holsapple, K. R. Housen, D. G. Korycansky, and K. Wünnemann. Validation of numerical codes for impact and explosion cratering: Impacts on strengthless and metal targets. *Meteoritics & Planetary Science*, 43(12):1917–1938, 2008.
- J.E. Richardson and S. Kedar. An experimental investigation of the seismic signal produced by hypervelocity impacts. In *Lunar and Planetary Science Conference*, volume 44, page 2863, 2013.
- Qicheng Sun, Guangqian Wang, and Kaiheng Hu. Some open problems in granular matter mechanics. *Progress in Natural Science - PROG NAT SCI*, 19, 05 2009. doi: 10.1016/j.pnsc.2008.06.023.
- NA Teanby. Predicted detection rates of regional-scale meteorite impacts on Mars with the InSight short-period seismometer. *Icarus*, 256:49–62, 2015.
- James H Tillotson. Metallic equations of state for hypervelocity impact. Technical report, General Dynamics San Diego CA. General Atomic Div., 1962.
- NH Warner, MP Golombek, J Sweeney, R Fergason, R Kirk, and C Schwartz. Near surface stratigraphy and regolith production in southwestern Elysium Planitia, Mars: implications for Hesperian-Amazonian terrains and the InSight lander mission. *Space Science Reviews*, 211(1-4):147–190, 2017.
- K Wünnemann, GS Collins, and HJ Melosh. A strain-based porosity model for use in hydrocode simulations of impacts and implications for transient crater growth in porous targets. *Icarus*, 180(2):514–527, 2006.
- Jerry A. Yamamuro, Paul A. Bopp, and Poul V. Lade. One-dimensional compression of sands at high pressures. *Journal of geotechnical engineering*, 122(2):147–154, 1996.
- Jerry A. Yamamuro, Antonio E. Abrantes, and Poul V. Lade. Effect of strain rate on the stress-strain behavior of sand. *Journal of Geotechnical and Geoenvironmental Engineering*, 137(12):1169–1178, 2011.
- Maria T Zuber, Sean C Solomon, Roger J Phillips, David E Smith, G Leonard Tyler, Oded Aharonson, Georges Balmino, W Bruce Banerdt, James W Head, Catherine L Johnson, et al. Internal structure and early thermal evolution of Mars from Mars Global Surveyor topography and gravity. *science*, 287(5459):1788–1793, 2000.

Appendix A: Example of Shot #13 data

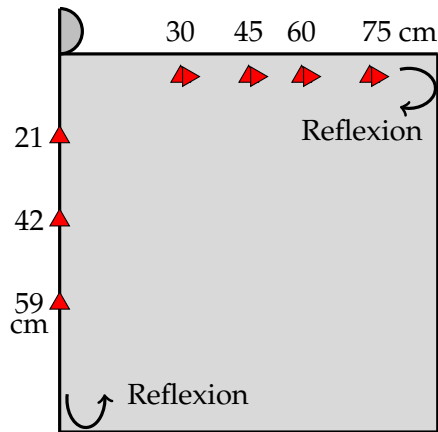


Figure 23 – Graphic of the vertical and horizontal sensors (impactor not to scale)

acceleration is $\pm 9 \text{ m/s}^2$ and the maximum velocity is -1.2 cm/s . The sensor is first pushed down by the pressure of the impact, accumulates deformation, and finally rebounds up with a maximum velocity of 0.9 cm/s . On these signals can be seen the arrival of the shock reflexion at the bottom of the tank (point R), the rebound of the sensor (from point RB), the elastic precursor (point E) and the plastic wave (P).

This appendix displays some experimental data of Shot #13 and illustrate how informations on the pumice material were retrieved from them.

Using the three vertical sensors and the four horizontal sensors that form a line radially from the impact point, it is possible to measure the shock wave velocity. Figures a and b show the propagation of the signal with distance. The propagation velocity was measured at $150 \pm 5 \text{ m/s}$ for the vertical sensors and $90 \pm 10 \text{ m/s}$ for the horizontal sensors.

Figures c (resp. d) show the acceleration (resp. velocity integrated from the acceleration) signals recorded 42 cm down the impact point. For this particular case, the shock wave arrives 2.65 ms after the impact and peaks at 4.2ms. The maximum

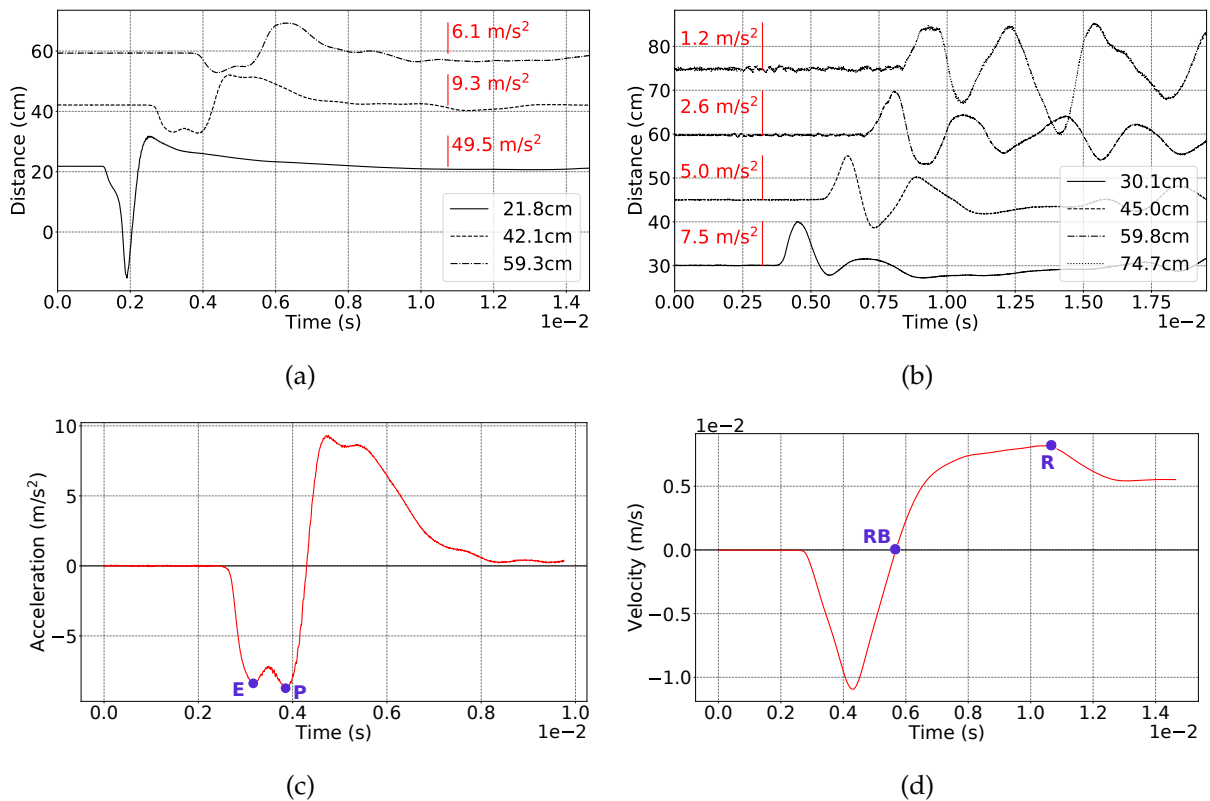


Figure 24 – (a) and (b) Wave arrival with distance at the vertical and horizontal sensors, in vertical and radial acceleration. Signals are normalised by the peak positive acceleration, and red lines indicate the peak amplitude. (c) (resp. (b)) Acceleration (resp. velocity) signals 42cm down the impact.